

PROPER MOTIONS OF BULGE STARS

Steven Gough-Kelly

A THESIS SUBMITTED IN PARTIAL FULFILMENT
OF THE REQUIREMENTS FOR THE DEGREE OF
MASTER OF SCIENCE

Jeremiah Horrocks Institute for Mathematics, Physics and Astronomy
University of Central Lancashire

December 2019

Declaration

Type of Award: Master of Science (by Research)

School: Physical Sciences and Computing

I declare that while registered as a candidate for the research degree, I have not been a registered candidate or enrolled student for another award of the University or other academic or professional institution.

I declare that no material contained in the thesis has been used in any other submission for an academic award and is solely my own work.

No proof-reading service was used in the compilation of this thesis.

Steven Gough-Kelly

December 2019

Abstract

Galactic bulges make up a significant portion of a spiral galaxies mass. Yet for a long period they have been generally understudied in comparison to the rest of the galaxy. The hardest galaxy to study is our own. Being in the plane, observations of the centre of the Milky Way (MW) is blocked by the stars and dust making measurements of its internal structures a challenge. To make predictions of the inner workings of the Bulge, star forming simulations are created to qualitatively compare the kinematics of the simulations and observations with the goal of inferring the formation mechanism of the MW bulge. This project was able to reproduce observed trends in chemically separated stellar proper motions within the MW with the age separated proper motions of a N-body+SPH simulation. This simulations bulge was formed through a kinematic fractionation process producing a Box/Peanut distribution. The results of this thesis give further evidence to the MW hosting a bar at its centre and a B/P bulge distribution formed through secular evolution.

Contents

Declaration	ii
Abstract	iii
Acknowledgements	ix
1 Introduction	1
1.1 Defining the Bulge Component	3
1.2 Box/Peanut Bulge Formation	5
1.3 Kinematic Fractionation	6
1.4 The Milky Way	9
1.5 Kinematics of Chemically Separated Bulge Stars	12
2 Simulation	15
3 Proper Motion Rotation Curves	19
3.1 Observational Fields	19
3.2 Simulated Fields	24
3.2.1 Longitudinal Proper Motion	28
3.2.2 Latitude Proper Motion	30
3.2.3 Radial Velocity	34
3.2.4 Age Dissection of Simulated Field	37

4	Velocity Maps of the Galactic Bulge	41
4.1	Current Observational Surveys	41
4.2	Proper Motion Maps	45
4.3	Velocity Correlations	53
5	Conclusions	55

List of Tables

3.1	The central latitude and longitude of the fields seen in Fig. 3.5. The number of stellar particles for each field and within each age bin: old ($Age \geq 9$ Gyr), intermediate ($6.5 \leq Age \leq 9$ Gyr) and young ($Age \leq 6.5$ Gyr) denoted as: N_* , N_o , N_i and N_y respectively along with the percentage of young stars within the field.	26
-----	---	----

List of Figures

3.1	The distribution of metallicity and age of the bulge population within the simulation. The cuts used to define three age populations are displayed by vertical lines. The average metallicity of each population: young (blue), intermediate (green) and old (red) is shown by dashed lines.	20
3.2	Longitudinal proper motion rotation curve of the simulated SWEEPS field, centred on $(l, b) = (+1^\circ, +3^\circ)$	21
3.3	BTS observational fields positions (stars) with their associated simulated field (black squares).	22
3.4	Longitudinal proper motion rotation curves of the simulated BTS Fields.	23
3.5	Positions of simulated fields for which proper motion rotation curves are produced (black squares). The BTS fields' positions for reference (stars).	25
3.6	The average number of stars along the line of sight of the simulated fields.	27
3.7	The average longitudinal proper motion rotation curve of the simulated fields.	29
3.8	The average dispersion in longitudinal proper motion along the line of sight of the simulated fields.	31

3.9	The average latitude proper motion rotation curve of the simulated fields.	32
3.10	The average dispersion in latitude proper motion along the line of sight of the simulated fields.	33
3.11	The average radial velocity rotation curve of the simulated fields. . .	35
3.12	The radial velocity against longitude at fixed latitude of $b = 2.5 \pm 0.25^\circ$.	36
3.13	The radial velocity against longitude at fixed latitude of $b = 5 \pm 0.25^\circ$.	37
3.14	The average dispersion in radial velocity along the line of sight of the simulated fields.	38
3.15	Longitudinal proper motion rotation curve of the simulated field centred on $(l, b) = (+1^\circ, +2^\circ)$ separated by stellar age.	40
4.1	X-Y density map of the central bulge for each population.	43
4.2	Maps of the proper motions and dispersions of the central bulge for all ages. Longitude proper motion (top left), dispersion of longitude proper motion (top right), latitude proper motion (bottom left) and dispersion in latitude proper motion (bottom right)	44
4.3	Maps of the average longitude proper motions of the three populations.	47
4.4	Maps of the average latitude proper motions of the three populations.	48
4.5	Maps of the average dispersion longitude proper motions of the three populations.	50
4.6	Maps of the average dispersion latitude proper motions of the three populations.	51
4.7	Maps of the average ratio of longitude proper motion dispersion to latitude proper motions proper motions of the three populations. . . .	52
4.8	Maps of the average correlation of longitude proper motion to latitude proper motions proper motions of the three populations.	54

Acknowledgements

“If you immediately know the
candle light is fire, then the meal
was cooked long ago.”

— Oma Desala

I would like to thank Victor Debattista for his continued supervision throughout this project. Your continued patience, guidance and encouragement has been instrumental in my progress to this stage and acted to inspire me to take on the next chapter of my academic career.

I would like to thank the members of the Galaxy Dynamics Research Group at the Jeremiah Horrocks Institute: Tigran, Leandro, Mark, Illin and David along with collaborators for their support and advice throughout this project.

Acknowledgement is also needed for Will Clarkson for his helpful insights during this project and conducting the initial research this work builds upon.

Furthermore my friends and colleagues of UCLan, the JHI, the Young Scientists Centre and UCLan Students' Union have provided countless opportunities to grow and develop as an individual and I wouldn't be who I am without them.

I wish to thank my family. There aren't enough words (even within a thesis) to show enough gratitude for being there every step of the way.

Finally to Xeng, the man who I give my life to. Forever.

Chapter 1

Introduction

The stellar bulges of disc galaxies constitute $\sim 25\%$ of all stellar light in the universe (Persic and Salucci, 1992; Fukugita et al., 1998). Furthermore, the bulge makes up approximately $1/5^{th}$ of a galaxy's stellar mass (Zoccali and Valenti, 2016). As such a major structure, it has been greatly understudied for a long time. However, as greater resolution telescopes and theoretical simulations have been developed, the less a simple power law definition has been able to account for observations of external galaxies. To be able to qualitatively compare any results we find during this project, the nature and current understanding of the bulges we observe in external galaxies must be reviewed.

To study the chemical evolution of a stellar system we consider a proxy for the full chemical composition of a star. Metallicity is defined as the logarithmic ratio of mass fraction of Iron (**Fe**) to Hydrogen (**H**) in a star relative to the Sun by Equation 1.1 where N_x is the number of atoms of element x per unit volume.

$$[\text{Fe}/\text{H}] = \log_{10} \left(\frac{N_{\text{Fe}}}{N_{\text{H}}} \right)_{\star} - \log_{10} \left(\frac{N_{\text{Fe}}}{N_{\text{H}}} \right)_{\odot} \quad (1.1)$$

A stellar system can be defined by an Initial-Mass-Function (**IMF**) which describes the initial distribution of mass in a the system. The first generation of stars

CHAPTER 1

have a metal-poor composition of mainly hydrogen and helium. Examples of old stars in the Milky Way are thick disc stars which have a metallicity of $[Fe/H] = -1$ making them ten times more metal-poor than the Sun. The lower mass stars of this system will remain over their long life and not change their metallicity significantly while evolving. However, the high mass stars undergo further evolutionary steps and produce a greater number of heavier elements in their core and will most likely end their much shorter lives in a supernova. The remaining gas which did not form stars in the system, the interstellar medium (**ISM**), is enriched by heavier elements through several processes. The first being the stellar winds of the red giant branch stars in the system, contributed to by primarily by the high mass stars. The gas can also be enriched through type Ia and type II supernova. This means the ensuing generation of stars form with a higher metallicity than the previous (Karttunen et al., 2017).

This process of enrichment produces a correlation between the age and metallicities referred to as an age-metallicity relation (**AMR**). For a simple system such as an isolated stellar system, this relationship is relatively simple. For systems such as high mass galaxies, the picture is not so clear. With star-formation not uniform across the entire galaxy and star formation rate not uniform throughout a galaxy's evolution, discrete age populations can have a range of metallicities. This also doesn't take into consideration gas accretion from the intergalactic medium (**IGM**) and merging events. A relationship between increasing age and decreasing metallicity is found for local stellar systems such as the Small and Large Magellanic Clouds (Piatti, 2012; Rubele et al., 2012, 2015; Bekki and Tsujimoto, 2012; Cignoni et al., 2013; Piatti and Geisler, 2013). This can also be seen in the Solar neighbourhood (Chiappini et al., 2001; Gibson et al., 2003)).

1.1 Defining the Bulge Component

Next considering the definition of the bulge component of a galaxy. When a galaxy is viewed edge-on the bulge is considered as a distribution of smooth light which protrudes out of the central disc. Due to low resolution observations, the distribution of the bulges of external galaxies were assumed to be smooth. Being a smooth distribution implies that there is little to no star formation or dust within the structure also indicating there is a single age population. In early research, the light profile fitted to this structure was the Sérsic profile: an $r^{1/n}$ law with commonly $n=4$ (Sersic, 1968; Athanassoula, 2005). The most commonly referenced galaxy which fits this definition is the Sombrero Galaxy (NGC 4594). However, as the quality and number of observations of galaxies increased as did the number of examples this definition did not fit.

Instead of easily modelled spheroidal bulges, observers found structures with peanut or box-shapes and bulges which display disc-like morphologies and kinematics such as inner spirals, rings, dust lanes and star-forming regions (Carollo et al., 1998). A pair of definitions were introduced by Kormendy and Kennicutt (2004) for bulges: classical bulges and pseudo-bulges. Classical bulges matching the previous definition of a smooth distribution. Their fast formation through gravitational collapse or through merging events in the formation period with other galaxies makes this bulge an older structure. They classified pseudo-bulges as disc-like structures arising due to the presence of a bar. With gas being accumulated at the galactic centre this can form a disc or ring which can undergo star formation producing a population of young stars in the bulge. The process of gas inflows to the galactic centre was studied by Cole et al. (2014). Still, this doesn't address the other observed bulges described as peanut or box-shaped.

Athanassoula (2005) presented definitions of bulges in three categories. The first being again the classical bulge. They also presented another classical bulge forming

CHAPTER 1

scenario of a gaseous proto-disc which is formed from the gravitational instabilities of material falling onto the early galaxy. Clumps of gas fall to the centre which merge to form a central bulge. This scenario was proposed by Noguchi (2000). The clumps fall quickly to the centre with a high amount of star-formation which leads to an old α -element rich population. This scenario also leads to a near $r^{1/n}$ density profile which matches the original bulge classification. The second definition is the Box/Peanut (B/P) bulge, sometimes referred to as an X-shaped bulge. These bulges are a product of secular evolution within barred galaxies which make up about 70% of disk galaxies (Eskridge et al., 2000). Secular evolution of this nature is slower than how classical bulges form. The bar forms within a few galaxy rotations. Following the bar formation, vertical heating transfers vertical motion to stars within the bar to greater heights above the disc. When the bar is viewed edge-on (with its major axis perpendicular to the line of sight) the bulge exhibits its signature shape. Due to it being formed from the stars present in the inner disc and vicinity of the bar, any stars formed in this region will become part of the morphology of this bulge. Therefore, the population of a B/P bulge will contain young stars although the majority of it can be constituted of old stars. The third type presented by Athanassoula (2005) is the Disc-like bulges. These match the Kormendy and Kennicutt (2004) definition of pseudo-bulges outlined above. Findings of such structures (nuclear discs/rings) both in simulation and in external galaxies have since been presented in recent studies (Portaluri et al., 2013; Cole et al., 2014; Debattista et al., 2015). These disc-like features being linked to galaxy bulges has been suggested by the previous work of Kormendy and Kennicutt (2004).

Even these robust definitions are not finite. The presence of a combination of these bulges is not impossible. Prugniel et al. (2001) argued that multiple bulges can exist with the same galaxy. This type of bulge is sometimes referred to as a compound bulge. This can affect the measured signatures of which bulge structures

are present (Cole et al., 2014). Galaxies observed at different rotations and inclinations can effect the interpretation of the bulge’s morphology. B/P bulges can appear spherical when viewed along the bar (end-on) and may only be detectable through kinematics (Erwin and Debattista, 2017).

1.2 Box/Peanut Bulge Formation

Both B/P and disc-like bulges are prerequisite by the formation of a bar. The high percentage of galaxies hosting a bar accounts for the frequency at which we find B/P bulges in external galaxies. Erwin and Debattista (2017) used a sample of 84 barred external galaxies to find what fraction have a B/P bulge. When doing this they found a mass dependence on the chance of forming a B/P. They also demonstrated that for galaxies of mass $\leq 10.4 M_{stellar}/M_{\odot}$ have a 79% chance of forming such a bulge whereas low mass galaxies have only $\approx 12\%$ chance. They were also able to correlate other mass-dependent properties of the galaxies (such as bar strength) to a formation chance. These structures are no longer expected to be mono-aged and have a range of ages through the migration of disc stars within the vicinity of the bar and through regions of star formation fuelled by gas inflows due to the bar (Cole et al., 2014). However, the young population may not be as extended as the older component when considering vertical heights above the plane (Ness et al., 2014).

Two processes that can vertically thicken the bar to give rise to the B/P shape. One is the bar buckling instability and the other being symmetric vertical thickening. Binney and Tremaine (2008) explained that bars “formed in thin disks rapidly evolve into thick structures that appear boxy when viewed edge-on, probably because they are unstable to buckling”. The higher horizontal velocity dispersion due to orbital motion along the bars major axis makes the bar more susceptible to the buckling instability than the surrounding disk (Raha et al., 1991; Binney and Tremaine, 2008; Debattista et al., 2006; Ness et al., 2014). It was theorised that bars may

CHAPTER 1

be weakened or even destroyed by this instability, however Debattista et al. (2006) found no cases in which the bar was destroyed in several different simulations with varying gas physics. Only cases where buckling resulted in very weak bars were found. They also noted that buckling does not always result in a peanut-shaped structure and not all bars buckle. At high enough central concentrations of gas, the buckling instability can be suppressed (Debattista et al., 2006). The buckling process has been observed in external galaxies and compared to simulation in a paper by Erwin and Debattista (2016). They were able to determine the timescale over which this event occurs. They showed that buckling is a quick process, on the order of ~ 1 Gyr.

Alternatively, the bar can also go through a slower process of symmetric growth. Stars on orbits which stream along the bar can become vertically thicker from being trapped on vertical resonances (Debattista et al., 2006; Quillen et al., 2013). The orbits which support the bar are found to be the x_1 family of orbits. The orbital families and their characteristics are explored in detail in Valluri et al. (2016). Abbott et al. (2017) showed that not one orbital family can explain the full extent of a B/P bulge morphology. Groups of non-resonant box and boxlet orbits all contribute to the observed shape. Erwin and Debattista (2017) found B/P bulges present in 80% of barred galaxies with gas mass ratios as high as 0.1. This is an indication of B/P bulges forming through this slow process as it is less dependent on the density of gas, unlike the buckling instability.

1.3 Kinematic Fractionation

Debattista et al. (2017) presented their findings of a process called kinematic fractionation. This is the separation of stellar populations with the same spatial distribution but different initial in-plane kinematics, due to the bar. To theoretically demonstrate kinematic fractionation they produced a pure N-body simulation with

CHAPTER 1

a single distribution function. This initial disc was then split into five separate populations with increasing in-plane velocity dispersions, but all have an identical density distribution referenced as D1 to D5 with D1 being the 'hottest' kinematically. They also produced two compound discs with combinations of the separate populations. One to approximate a galaxy with uniform star formation rate through its life (equal combination) and one to approximate a declining star formation history (5:4:3:2:1 ratio of D1:D2:D3:D4:D5). This produced a disc with a high population of old stars compared to young stars. The full simulation parameters are discussed within the paper. When viewed separately, after a period of evolution, disc D1 shows the most rapid increase in average vertical height before the bar even forms as a trade-off for a decrease in average radial velocity dispersion. The bar amplitude increase slowly only after the average radial velocity dispersion has ceased decreasing but never produces a strong bar. However, the coolest disc, D5 slowly increases its vertical distribution as its average radial velocity dispersion increases along with the bar strength until eventually the bar buckles. The buckling event rapidly increases the average vertical height and decreases both average radial velocity and bar strength.

This result showed that the evolution of a population is heavily dependent on the initial radial velocity dispersion before the disc forms a bar. If a disc is comprised of both 'hot' and 'cold' (kinematically) populations the hot will act to thicken the disc rapidly and lose its radial velocity dispersion without forming a strong bar. The cold component drives the formation of a strong bar which can buckle leading to vertical thickening of younger populations and the increase in radial velocity dispersion. Compound discs more closely resemble real galaxies we observe. Both compound discs explored by Debattista et al. (2017) showed qualitatively similar trends. A bar forms less rapidly than the D1 disc and grows to form a strong bar while vertical height slowly increases. Peak bar strength is seen to have an anti-correlation with initial radial velocity dispersion. The bar then buckles giving a

CHAPTER 1

rapid increase in average vertical height. Prior to buckling the hottest population had the largest increase in vertical height. This population remained the one with the largest vertical height after buckling.

These pure N-body simulations show that bar evolution can drive the vertical thickening of the inner disc. Stellar populations with greater initial radial velocities end up with a greater average vertical height above the plane than populations with cooler initial radial velocities. The hotter population trace a more spheroidal shape contrary to the peanut-shaped produced by the cooler population. This demonstrates that initial radial velocities are the determining parameter for the morphology of the resulting bulge.

Debattista et al. (2017) then progressed onto exploring if this theory holds to for a high-resolution N-body+Smooth Particle Hydrodynamics (SPH) simulation which forms a bar-spiral galaxy completely from gas. The full details of this model will be outlined in the next chapter. As an overview, this simulation forms a disc galaxy from a gas corona eventually forming a strong bar, a nuclear disc and a B/P shaped bulge (Cole et al., 2014; Ness et al., 2014; Debattista et al., 2015, 2017). The chemistry of the gas is enriched through the feedback of asymptotic giant branch stellar winds, type Ia and type II supernova. The velocities and spacial components are scaled to approximate the Milky Way. The observers location is placed to match the Suns position within the Galaxy.

Considering the simulation throughout its evolution, the oldest stars exhibited the greatest radial velocity dispersion compared to the youngest stars. They were also able to show correlations between both metallicity (anti-correlation) and α -abundance with radial velocity dispersion before the bar is formed. This would imply the same kinematic process will apply to these correlations and embed these physical properties in the final morphology of the bulge as the bar evolves. It also suggests there will be a kinematic difference between populations separated by the

CHAPTER 1

same physical properties. There was no strong buckling event in this simulation, however it did undergo continuous vertical heating through symmetrical growth.

Like the pure N-body simulations, they are able to see a separation in populations when measuring average vertical height. Metal poor populations extend to the greatest vertical height and increase steadily with radius from the galactic centre. The metal-rich population do not reach the same vertical height but exhibits a local peak at approximately $R \approx 1.6$ kpc interpreted as the signature of a peanut-shaped distribution. These differences in average vertical height embedded a vertical metallicity gradient within the galaxy. This is seen in the 2D maps of the galaxy centre (figure 24 Debattista et al. (2017)). Young metal-rich stellar particles form a stronger bar and more closely trace the X-shape compared to the old metal-poor stellar particles. If the connection between old stars having high initial radial velocity dispersion is made and young stars having low radial velocity dispersion, the star-forming simulation is in agreement with the pure N-body ones.

1.4 The Milky Way

In reference to the Milky Way having a measured mass of $5 - 6.5 \times 10^{10} M_{\odot}$ (McMillan and J., 2011a, 2016) it is possible to refer back to Erwin and Debattista (2017) and place the Milky Way on the mass B/P bulge probability relationship and find that the Galaxy has a 0.79 – 0.88% chance of forming a B/P bulge. This implies it would be unlikely that the Milky Way did not develop one.

These theoretical considerations all contribute to how we can interpret observations and measurements of external galaxies as well as our own galaxy. Proposals for the Milky Way hosting a bar came as early as the 1960s which were later reinforced with more evidence in the following decades (de Vaucouleurs et al., 1964; Gerhard and Vietri, 1986; Binney et al., 1991, 1996; Stanek et al., 1994, 1996). This allows for the internal processes such as kinematic fractionation to occur and the

CHAPTER 1

morphology be susceptible to the processes which give rise to B/P shaped bulges. Binney et al. (1996) used data from the Diffuse Infrared Background Experiment **DIRBE** on-board the Cosmic Background Explorer (**COBE**) to estimate the bar pattern speed and inclination angle of the bar to the line-of-sight from the Sun to be $\Omega_b = 60 - 70 \text{ km s}^{-1} \text{ kpc}^{-1}$ and $\alpha \sim 20^\circ$.

To be able to determine the shape of our Galaxy's inner structure stellar distances are needed. One way is to use standard candles, stars we theoretically know the absolute luminosities of, to determine distances through photometry. The measured apparent magnitude (brightness) is compared to its known absolute magnitude through the distance modulus equation. Most commonly these stars are red clump (**RC**) stars. These tend to form an over-density on the horizontal red giant branch of a Hertzsprung-Russell diagram (**HRD**), or observationally, colour-magnitude diagram (**CMD**). Their evolution is discussed in Girardi (1999) and references within. They are used as standard candles as their absolute luminosities are insensitive to their age or metallicity (Girardi and Salaris, 2000). The observation of these stars within the Milky Way has been used by previous work to determine the barred nature of the Galaxy in Stanek et al. (1996) and Stanek et al. (1997). It has also been used to estimate the distance to the galactic centre given as $R_0 = 7.52 \text{ kpc}$ (Nishiyama et al., 2006).

Gonzalez et al. (2011) measured two components of the Milky Way bulge. One metal-poor which formed fast and early which possibly comes from merging events along with a metal-rich component which becomes less dense at increasing latitudes suggesting a component formed over a much slower period. This also gives rise to a measurable metallicity gradient which is one signature of a B/P bulge presented in Debattista et al. (2017). Kinematic fractionation allows for the gradient to be a product of internal evolution without the need for a gradient in the initial system.

Early measurements of the Galactic bulge utilised Optical Gravitational Lensing

CHAPTER 1

Experiment (**OGLE**) and Two Micron All-Sky Survey (**2MASS**) survey data of RC stars to detect the X-shaped structure as a signature of a B/P bulge (Stanek et al., 1996; Rattenbury et al., 2007a,b; Nataf et al., 2010; McWilliam and Zoccali, 2010; Saito et al., 2011a). At higher latitudes the RC density along the line of sight produced a bimodal distribution seen in Gonzalez et al. (2011) which is expected when looking through the X-shape of the bulge. In contrast, Pietrukowicz et al. (2014) showed that metal-poor RR Lyrae stars have a more spheroidal distribution. Wegg and Gerhard (2013) built upon this previous work with DR1 data from the Vista Variables in the Via Lactea (**VVV**) survey covering a wide field of the Galactic centre and exploring fainter targets allowing for deeper observations close to the plane (Saito et al., 2011b). Assuming an eight-fold symmetry within the Galaxy, Wegg and Gerhard (2013) were able to produce three-dimensional density maps of the centre to reveal a bar at an angle of $\alpha = 26.5^\circ$ to the line of sight. With the same technique, they also produced a projection of the bulge side-on which shows a clear B/P shaped distribution.

Debattista et al. (2017) employed similar methods to measure the bulge in the star formation simulation, building upon previous work done with the same simulation in Gonzalez et al. (2015). They create a simulated sample of RC stars and separate them by age, presenting the line of sight distributions. They showed younger RC stars displaying a bimodal distribution and older RC stars showing only a single central peak. This matches both predictions of kinematic fractionation, separating the morphology of differently ages populations, and the signature of a B/P bulge.

Zoccali et al. (2017) used spectral observations from the GIRAFFE Inner Bulge Survey (**GIBS**) taken with the Very Large Telescope **VLT** within the field of view of the VVV survey. The metallicity distribution function (**MDF**) of the 26 fields studied in this paper show clear bimodalities. They demonstrated that a metal-rich

CHAPTER 1

component of the bulge dominates at latitudes close to the plane and a metal-poor component at high latitudes. The mixing of these two components creates a vertical metallicity gradient. By interpolating their data, they were also able to create maps of the galactic centre from their sample. Two populations were created by splitting the RC stars into a metal-rich and a metal-poor population. The metal-rich stars have a boxy morphology and are less centrally concentrated compared to the more spherical and centrally concentrated metal-poor stars. There is also a greater number of metal-poor stars. The density of metal-rich stars drops at high latitudes. To look for evidence of a difference in kinematics between the two populations, this study presented Galactocentric radial velocities as a function of longitude at fixed latitudes. Although not a strong separation they were also able to detect that metal-rich stars rotate slightly faster than metal-poor stars.

1.5 Kinematics of Chemically Separated Bulge Stars

Clarkson et al. (2018) studied the Galactic bulge using Hubble Space Telescope (**HST**) archive images. Photometry of main sequence (**MS**) stars were measured and their proper motions determined using the Advanced Camera for Surveys Wide Field Camera **ACS/WFC**. Follow up photometry data from the Bulge Treasure Survey **BTS** taken with the ACS/WFC on board the HST was used in 3 bands to create a temperature index (F390W, F555W and F814W) and a further 3 to create a metallicity index (F555W, F110W and F160W). This allows a metallicity value to be attached to each star based on its photometric measurements without the need for spectroscopic data which in high-density fields is less effective and limits the amount of data available. This approach allows for a large data set with less bias towards higher magnitude limits. The Sagittarius Window Eclipsing Extrasolar Planet Search (**SWEEPS**) is a survey conducted in 2006 of 180000 stars to detect exoplanets. The significance of this field is that it has lower levels of

CHAPTER 1

dust and extinction than other fields this close to the galactic centre (Clarkson et al., 2007). Other such windows have the potential for similar analysis: Stanek's Window, Baades Window and OGLE29 (Stanek et al., 1997; Kuijken and Rich, 2002; Sumi and Takahiro, 2003).

The sample used by Clarkson et al. (2018) is composed of the overlapping fields of the ACS/WFC and BTS WFC3 data. The resulting field is approximately $3' \times 3'$ centred at $(l, b)_{J2000.0} \approx (+1.26^\circ, -2.65^\circ)$. The distance is determined through relative photometric parallax based on the fields colour-magnitude diagram. A distance to the Galactic centre is taken from Calamida et al. (2014) as $D = 7.76$ kpc. Being able to tag stars with a metallicity meant they were able to produce two populations: a metal-rich and a metal-poor sample. The proper-motion rotation curves of the two populations were then produced. No rest frame tracers were used so the proper motions are relative and given an arbitrary zero point.

Their main results are that, when considering proper motion in galactic longitude, μ_l , the metal-rich sample exhibit greater amplitude proper motion, with a steeper gradient through the Galactic centre than the metal-poor. In galactic latitude, μ_b , no statistically significant difference between near and far side was detected. However, the separation in longitude is enough to determine that these two populations are separable by their kinematics. This also demonstrates that imposing object selections based on proper motions (traditionally $\mu_l < -2.0 \text{ mas yr}^{-1}$ is marginally biased towards metal-poor objects, thus making kinematic measurements of external galaxies and clusters sensitive to this and leading to the misinterpretation of the chemistry of stellar populations. Clarkson et al. (2018) also go on to summarise that this method can be applied to other BTS survey fields.

This project is undertaken under the rationale that the trends found by Clarkson et al. (2018) are a signature of the Milky Way having undergone kinematic fractionation due to the dynamical processes of its bar. To make this link, the project aims

CHAPTER 1

to study the same star-forming simulation outlined in Debattista et al. (2017) for the separation of kinematics in different populations and make predictions for future observational studies of this nature. The project's secondary aim is to compare large scale observations of the bulge to determine if similar structures are found in both proper motions and correlations of proper motion components when compared to observational data.

This thesis is constructed as follows: Chapter 2 will summarise the primary simulation used in this project. Chapter 3 will present the work done to reproduce the trends seen in Clarkson et al. (2018) and investigate the trends seen in other observational fields. Following that will be an analysis of simulated wider fields within the galactic centre to inform observations not already conducted. Chapter 4 will be the analysis of proper motion maps of the Galactic centre, comparing them to recent observational surveys. In Chapter 5 the main findings will be discussed, and the conclusions presented.

Chapter 2

Simulation

In this project a high-resolution N-body+SPH star-forming simulation which forms a disc galaxy from a hot gas corona is analysed. The simulation begins with 5 million dark matter particles to create a dark matter halo. The dark matter particles have a force softening of $\epsilon = 103pc$ and forms a halo with virial radius of $r_{200} = 198$ kpc and virial mass of $M_{200} = 9.0 \times 10^{11} M_{\odot}$. Embedded in this dark matter halo is a pressure supported corona of 5 million gas particles with a force softening of $\epsilon = 50pc$. These particles are initially in pressure equilibrium. The gas is given an angular momentum with $L_z \propto R$ to produce a spin parameter of $\lambda \approx 0.041$. Where λ is defined as:

$$\lambda = \frac{J|E|^{\frac{1}{2}}}{GM^{\frac{5}{2}}} \quad (2.1)$$

This technique has been previously proven effective in studying the evolution of disc galaxies by Roškar et al. (2007) and Roskar and Debattista (2012) as an alternative to previous works based on made to measure simulations with hand-placed stellar components (Sellwood and A., 1985; Fux and R., 1997, 1999; Martinez-Valpuesta and Gerhard, 2011; Saha et al., 2010; Ness et al., 2012; Gardner et al., 2013).

CHAPTER 2

At the beginning of the simulation, no stellar particles exist. It is evolved through the N-body+SPH code GASOLINE (Wadsley et al., 2003) with a base time-step of 10 Myr. The gas in the corona cools and settles to the centre forming a disc. If densities of gas grow greater than 100 amu cm^{-3} with a temperature of $T < 15000\text{K}$, star formation is triggered. Ten per cent of the gas particles in this state form stellar particles with thirty-five percent the mass of the gas particles they are born from. The stellar particles have mass equal to $\approx 9.4 \times 10^3 M_{\odot}$. The gas particles in this state will continue to spawn stars until their mass falls to below twenty-one per cent of their initial mass. The remaining mass is redistributed to its nearest neighbours and the gas-particle is removed. Each stellar particle is a representation of an IMF. In this case we assume a Miller-Scalo exponent of $\alpha = 1$. The coronal gas starts with pure hydrogen and helium ($[\text{Fe}/\text{H}] = -4$). For the chemical enrichment of the gas particles, the *blastwave* prescription of Stinson et al. (2006) is used. Feedback from asymptotic giant branch stellar winds, type Ia and type II supernovae all contribute to the enrichment of the ISM. The theoretical yields of the enrichment within the ISM with iron and oxygen is taken from Woosley and Weaver (1995). This simulation does not include a black hole at its centre so there is no feedback from an active galactic nucleus. The diffusion of metals between gas particles (Loebman et al., 2010) was not used in this simulation. This has the effect of producing low metallicity stars at all ages, broadening the metallicity distribution. Debattista et al. (2017) were able to demonstrate that the alternate feedback methods outlined above were still able to closely match the metallicity distribution functions generally across the Milky Way however local analysis of small samples show much weaker relationships. The age-metallicity relationship is also broadened by migration, however, due to the simulation evolving in isolation there is no broadening from merging and accretion events.

The simulation is evolved for 10 Gyr by which stage a disc galaxy has formed

CHAPTER 2

with a stellar mass of $\sim 6.5 \times 10^{10} M_{\odot}$ contained within $\sim 1.1 \times 10^7$ particles. This is simulated spiral galaxy qualitatively similar to the Milky Way, however, the scale of the disc and the bar formed in this simulation are smaller. The disc formed in the simulation is only $R_d \approx 1.7$ kpc whereas observations put the Milky Ways disc length at $1.8 \leq R_d \leq 4.0$ kpc (Ojha and K., 2001; Chang et al., 2011; McMillan and J., 2011b). The bar in the simulation forms at $t \sim 3.2$ Gyr and peaks in strength at $t \approx 5.2$ & 5.8 Gyr (Cole et al., 2014). Bar strength is defined by the amplitude of the global $m = 2$ Fourier moment (Debattista and Sellwood, 2000). By 10 Gyr the bar is ~ 3 kpc long which again is shorter than observations of the Milky Ways bar at ~ 3.5 kpc Robin et al. (2011).

A B/P bulge is measured within the simulation (Ness et al., 2014; Cole et al., 2014; Gardner et al., 2013; Debattista et al., 2017) and due it being formed in isolation all the processes leading to this morphology are internal. However, Debattista et al. (2017) mentioned that the X-shape this model produces is likely weaker than the Milky Way due to the simulations smaller bar length. A nuclear disc can also be seen within a kiloparsec of the centre of the simulation formed through high rates of gas inflow (Cole et al., 2014).

To approximate the Milky Way, we centre the simulation using the python package *pynbody* which centres using an initial guess based on the particle with the lowest potential and is then refined using the shrinking sphere method Pontzen et al. (2013). The simulation is then spatially scaled by a factor of 1.2 and the velocities are scaled by 0.48 bringing its bar size to 3.6 kpc. The observers position is placed 8 kpc away from the simulation centre to be in line with observational estimates (Gillessen et al., 2008; Wegg and Gerhard, 2013; Qin et al., 2018). The bar is aligned to 27° to the line of sight of the observer to the galactic centre with the near side of the bar at positive longitude (Wegg and Gerhard, 2013). The proper motions of each stellar particle are then calculated using the routines of the *galpy*

CHAPTER 2

(Bovy and Jo, 2014) python package without corrections for solar motion which puts the measurements in the galactic rest frame. This is done to maintain an unbiased view of the centre of the simulation without the artefacts of different observational methods and measurements.

Chapter 3

Proper Motion Rotation Curves

3.1 Observational Fields

For the initial analysis, the SWEEPS field studied in Clarkson et al. (2018) was considered first. The field is centred on $(l, b)_{J2000.0} \approx (+1.26^\circ, -2.65^\circ)$ with a field of view of approximately $3.4' \times 3.4'$. When the field is matched exactly within the simulation, only a few hundred stellar particles are within the field, which after separating by distance, was not enough to conduct a statistically significant study. To combat this, the field size was increased to $30' \times 30'$. The simulation is also assumed to have one-fold symmetry about the plane, therefore stars with $z < 0$ were projected onto $z > 0$ with an inverted vertical velocity ($v'_z = -v_z$, for $z < 0$) and the proper motions were recalculated. This gives a much larger sample of stellar particles within the field.

As noted in the previous chapter, the simulation does not include metal diffusion between gas particles. This serves to mix populations which could normally be separated within small spatial regions. Instead, this project separated populations into three age bins. A young population defined by $\text{age} < 6.5$ Gyr, an intermediate population $6.5 < \text{age} < 9$ Gyr and an old population $\text{age} > 9$ Gyr. It is then possible to associate the young population with metal-rich stars and the old population with

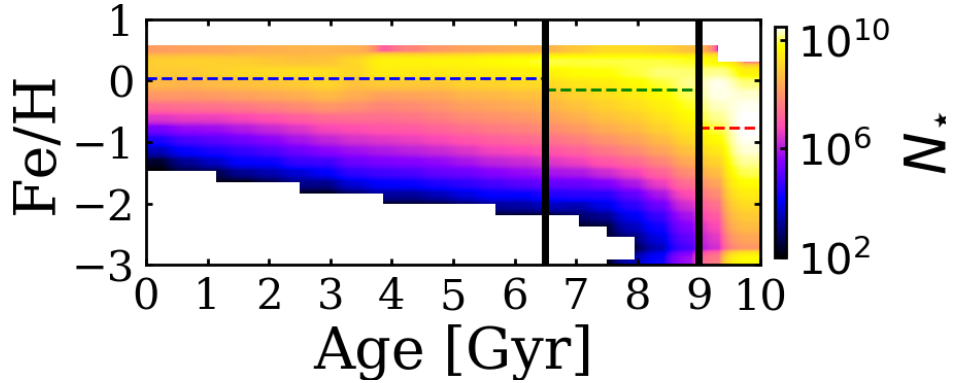


Figure 3.1: The distribution of metallicity and age of the bulge population within the simulation. The cuts used to define three age populations are displayed by vertical lines. The average metallicity of each population: young (blue), intermediate (green) and old (red) is shown by dashed lines.

metal-poor stars. From this point, the stellar particles within the simulation will be referred to as stars. Figure 3.1 shows the distribution of metallicity as a function of age of the bulge population. The age cuts are shown with the value of the average metallicity of each population. The young, intermediate and old populations have metallicities of -0.15, -0.23 and -0.81 respectively. This reinforces why this project separates by age. Distance ranges of 6 kpc to 10 kpc are split into 15 bins where the proper motions of the stars within the bin are averaged.

The longitude proper motion rotation curve of the SWEEPS field is shown in Figure 3.2. In all populations, the proper motion rises on either side of the galactic centre at 8 kpc. Bins with $d < 8$ kpc show positive proper motion whereas bins with $d > 8$ kpc show negative proper motion. This indicates the simulation is rotating clockwise from our observers perspective. The maximum proper motion is larger than the minimum in all three populations most probably due to the perspective affect of the measurements. The young population clearly demonstrates a higher amplitude proper motion than the other populations. It also has a steeper gradient through the galaxy centre. This is consistent with the finding of Clarkson et al.

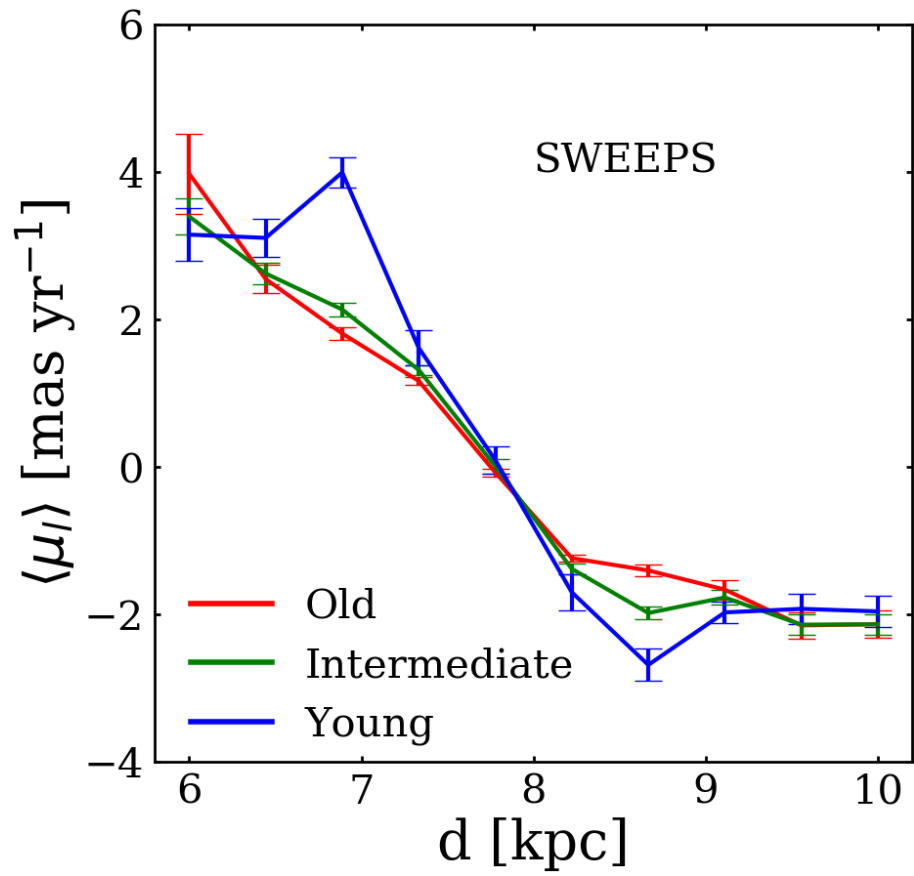


Figure 3.2: Longitudinal proper motion rotation curve of the simulated SWEEPS field, centred on $(l, b) = (+1^\circ, +3^\circ)$.

CHAPTER 3

(2018). The amplitude and gradient ratios of the young stars are greater than the old stars by a factor of $A_y/A_o \approx 2$. Through the centre the young population have a gradient of $m_y = -3.75 \text{ mas yr}^{-1} \text{ kpc}^{-1}$ whereas the old population have a gradient of $m_o = -1.99 \text{ mas yr}^{-1} \text{ kpc}^{-1}$ which results in a gradient ratio of $m_y/m_o = 1.88$. This is lower than that observed by Clarkson et al. (2018). The intermediate-age population follows the older population more than the young population. The average age of the intermediate population is 8 Gyr, due to a high number of old stars within the bulge. Although, they do show marginally greater amplitude proper motion than the old population. This indicates that potentially only a few Gyr difference in age is enough to separate the populations kinematics. One noticeable difference between these results and Clarkson et al. (2018) is that in the nearest and furthers distances the paper was able to show a clear separation between the metal-rich and metal-poor populations however our populations at the same distances converge again after separating.

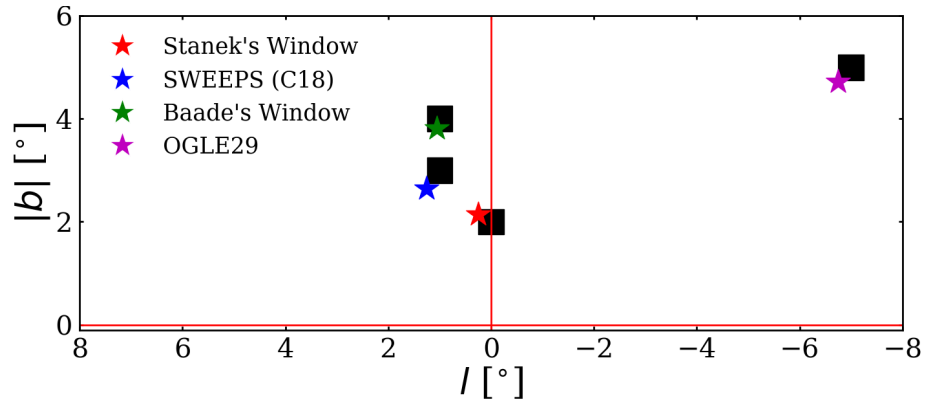


Figure 3.3: BTS observational fields positions (stars) with their associated simulated field (black squares).

As mentioned in the Chapter 1, three other fields surveyed by the BTS survey are potential candidates for this type of analysis. The simulated field positions are shown in Figure 3.3 with their centres represented with absolute latitude. The field

CHAPTER 3

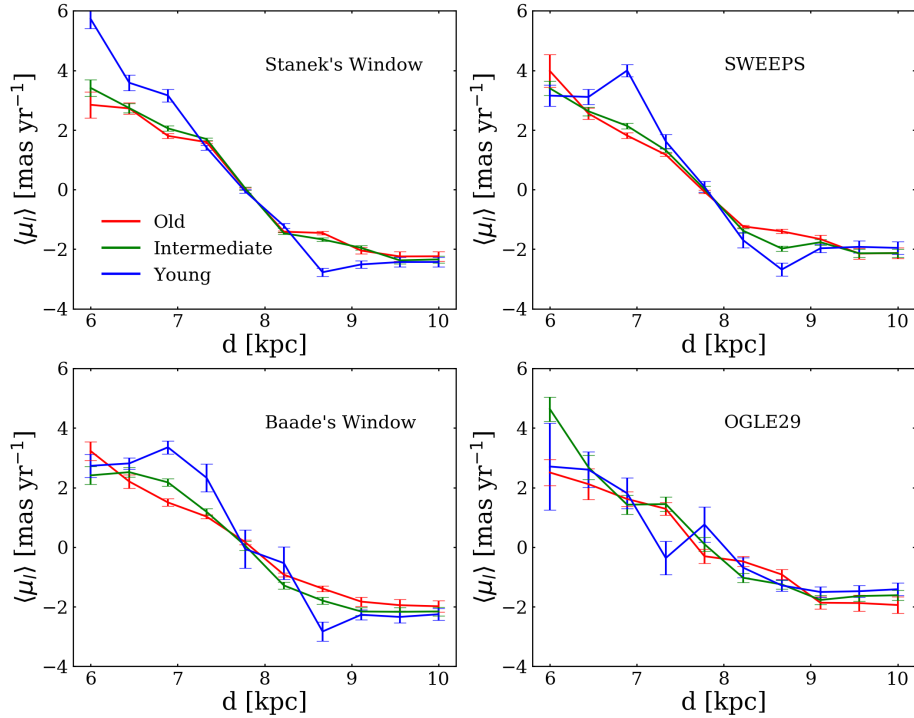


Figure 3.4: Longitudinal proper motion rotation curves of the simulated BTS Fields.

sizes are again increased to $30' \times 30'$ and positions are shown by the black squares within the figure. The same distance limits and bins are applied to the fields. These results are not meant to be quantitative predictions for what observers will find if these studies are conducted, they will act as a qualitative informant of trends to be expected. Three fields out of the four reside relatively central within the Galaxy but have varying latitude. The OGLE26 field is at a significantly larger longitude and is at the largest latitude. This is shown to be one of the greatest factors within the four fields proper motion rotation curves.

All four simulated BTS fields are presented in Figure 3.4. Both Stanek's and Baade's Windows show qualitatively similar trends to that of the SWEEPS field with increasing proper motion from the galactic centre. The youngest population again demonstrates the greatest amplitude in proper motion with the intermediate-age population remaining close to the old population. Stanek's Window does not

CHAPTER 3

show a separation in gradient through the galactic centre. However, at the closest distance bin the young and old population have not converged. This more closely resembles the findings of Clarkson et al. (2018). Staneks Window represents the lowest field of the four. The three fields excluding the OGLE29 field show higher amplitude proper motions in the nearest peak when compared to the furthest with an amplitude ratio of approximately $A_{near}/A_{far} \sim 2$. This is again due to the perspective effect of looking at an angled line of sight along with greater distances reducing the amplitude of proper motions (Qin et al., 2015). The OGLE29 field does not follow any of the previous trends. It demonstrates a roughly linear relationship between longitude proper motion and distance crossing the galactic centre for all three populations. The region covered by this field may miss the X-shape of the B/P bulge within the simulation and is considerably further from the galactic centre so shows less separation.

Examining the galaxy using the four observational fields gives an indication of variation in the longitudinal proper motion rotation curves with varying field position. They also indicate that the separation of population kinematics is not detectable across the entire central bulge.

3.2 Simulated Fields

To uncover how the separations of proper motions within different populations vary across the bulge of the simulation, an expanded search is conducted. An array of fields both at positive and negative longitudes were created, covering an area of $-6^\circ < l < 6^\circ$ and $0^\circ < b < 5^\circ$. This allows for a test of asymmetry from left to right and the determination of any vertical trends. The field size remained the same with the previous analysis of $30' \times 30'$, $6 \leq d \leq 10$ kpc and 15 bins in distance. Figure 3.5 displays the position and size of each of the sixteen fields. Fields with high longitude and high latitude values have not been included as from the results of the simulated

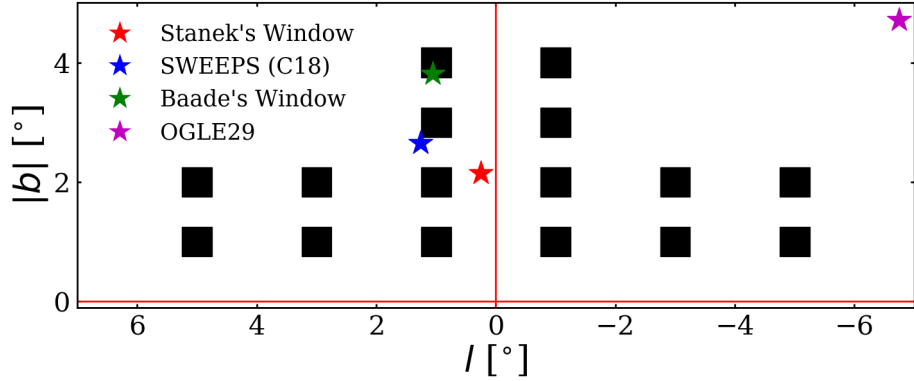


Figure 3.5: Positions of simulated fields for which proper motion rotation curves are produced (black squares). The BTS fields’ positions for reference (stars).

OGLE29 field showed no separation of population kinematics would be found.

Again, the stars in each field were split into three age bins: old, intermediate and young with cuts on age at 6.5 Gyr and 9 Gyr. The contribution of each population to the total number of stars for each field is shown in Table 3.1.

Table 3.1 shows clearly that the highest latitude fields have a factor of 4 times fewer young stars than in the lower fields. However, the young population still only contributed at most 20% at low fields demonstrating the dominance of old stars within the bulge. The density of the fields increases with decreasing latitude as expected.

To discover how the density of stars changes along the line of sight, the number of particles was plotted against distance using the same bins as above (Figure 3.6). In each field, the dominance of old stars is evident with the exception of the lowest, most central fields. In fields at latitudes $|b| \leq 2^\circ$, the young stars exhibit a narrower peak at 8 kpc compared to the intermediate and old populations. This is most likely the signature of the young stars’ stronger bar (Debattista et al., 2017). The fields at positive longitude show higher density in the nearest distance bin than the furthest

CHAPTER 3

(l, b)	N_{\star}	N_o	N_i	N_y	$\frac{N_y}{N_{\star}}$ (%)
(1,4)	5783	3452	1999	332	5
(-1,4)	5817	3486	1945	386	6
(1,3)	15097	9180	5144	773	5
(-1,3)	14895	9061	5013	821	5
(5,2)	10112	4880	4152	1080	10
(3,2)	23772	12549	9515	1708	7
(1,2)	40160	22021	14162	3977	9
(-1,2)	40739	22050	14588	4101	10
(-3,2)	24806	12764	10032	2010	8
(-5,2)	10179	4812	4224	1143	11
(5,1)	15278	6599	6278	2401	15
(3,1)	38143	17246	15588	5309	13
(1,1)	78207	34412	28237	15558	19
(-1,1)	80731	35089	29634	16008	19
(-3,1)	40298	17822	16613	5863	14
(-5,1)	15587	6561	6350	2676	17

Table 3.1: The central latitude and longitude of the fields seen in Fig. 3.5. The number of stellar particles for each field and within each age bin: old ($Age \geq 9$ Gyr), intermediate ($6.5 \leq Age \leq 9$ Gyr) and young ($Age \leq 6.5$ Gyr) denoted as: N_{\star} , N_o , N_i and N_y respectively along with the percentage of young stars within the field.

CHAPTER 3

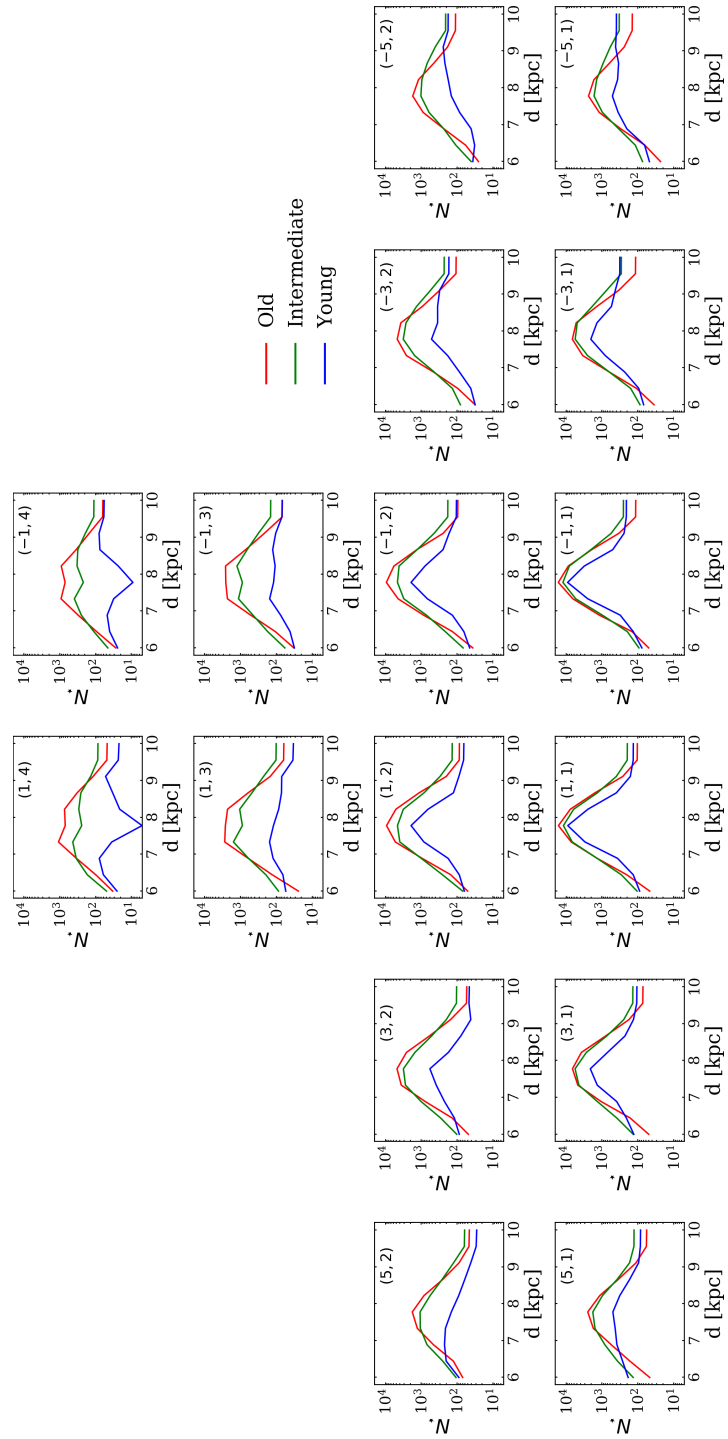


Figure 3.6: The average number of stars along the line of sight of the simulated fields.

CHAPTER 3

distance bin. At negative longitude, the opposite is seen. This is interpreted as the higher density due to the presence of the bar at an inclined angle. For fields $|b| \geq 2^\circ$, all 3 populations show traces of bimodality with two peaks at 7 kpc and 9 kpc, most strongly seen in the youngest population. There is noticeable difference between the old and intermediate distributions which shows again a few giga-years is enough time for different populations to develop different morphologies. This figure also demonstrates that each distance bin has a dense enough sample to analyse the kinematics of each population sufficiently.

3.2.1 Longitudinal Proper Motion

Figure 3.7 shows the longitudinal proper motion rotation curves of the theoretical fields. Almost all the fields match qualitatively the findings from Clarkson et al. (2018). Those which don't, are at the largest longitude values ($|l| = 5^\circ$). These fields are similar to the simulated OGLE29 field in that they show very little separation of populations. However, at positive longitudes, distance bins beyond the galactic centre show a slight separation of the young population from the intermediate and old. This would indicate separations preceding the bar. At negative longitudes, the separation is seen in the nearest distance bins before the galactic centre, again preceding the bar. This is potentially the influence of the nuclear disc. At central longitudes and low latitudes, clear separations can be seen with the populations not converging again at the nearest and furthest distance bins, as seen in Clarkson et al. (2018). This highlights the qualitative difference between this simulation and the Milky Way. The simulation's bar and evolution are not an exact match for the Milky Way which can account for these subtle differences. The central fields at all latitudes show between the two peaks an amplitude ratio of $A_{near}/A_{far} \sim 2$. The difference in the gradient of the rotation curves between old and young stars is not observed in many fields. However, the separation seen in the SWEEPS

CHAPTER 3

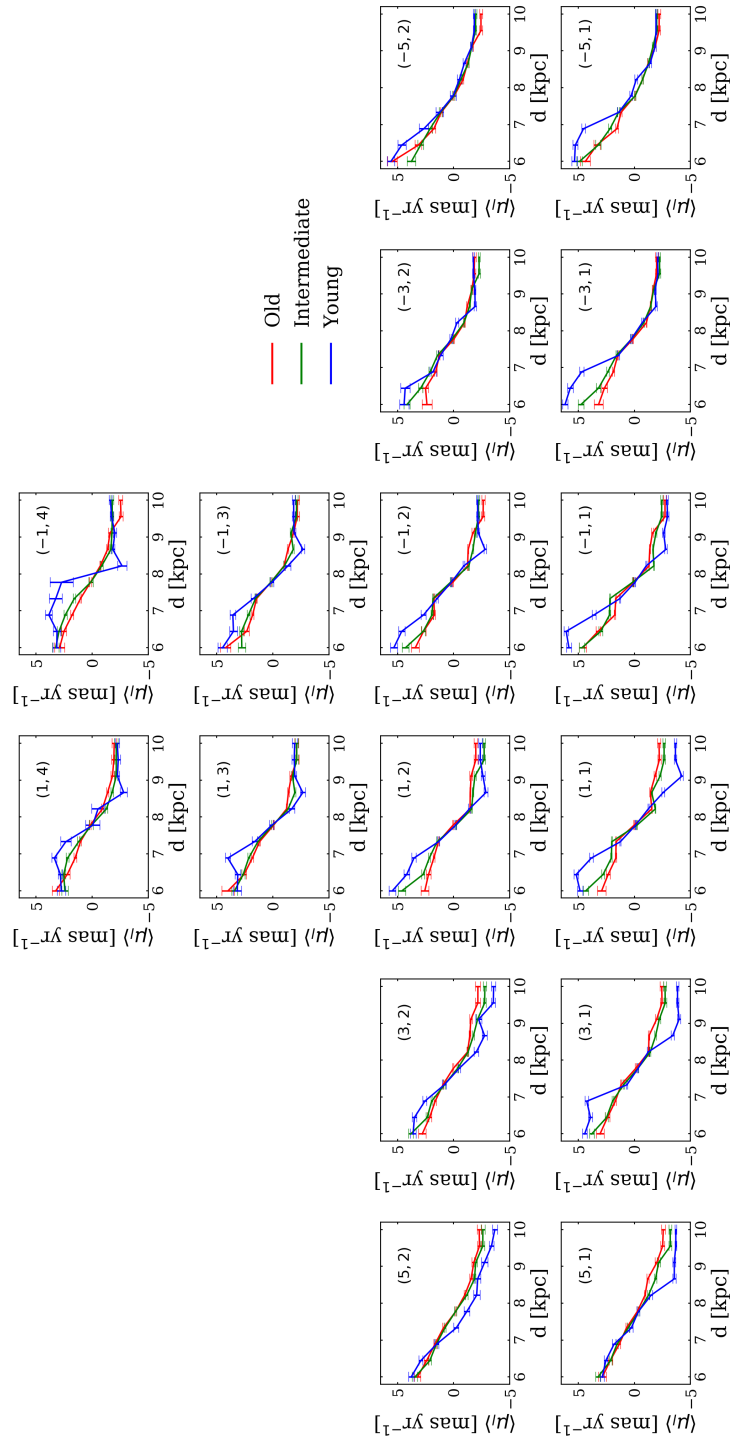


Figure 3.7: The average longitudinal proper motion rotation curve of the simulated fields.

CHAPTER 3

field is only $m_y/m_o \sim 2$. The strength of this signature may be dependant on more subtle structuring within the central bar which will be hard to replicate in a qualitative model. As seen previously the intermediate-age stars closely trace the old population.

The dispersion in longitudinal proper motion along the line of sight shown in Figure 3.8. For almost all the fields each profile has consistent key features across all populations. The nearest distance bin has a greater amplitude than the furthest, which is expected from previous works by Qin et al. (2015). The peak dispersion is found close to the galactic centre. At low and central fields, the old and intermediate-age populations are seen to have larger amplitude dispersion peaks at the galactic centre. Valenti et al. (2015) presented an interpretation of the central dispersion peak within the Milky Way. Investigating RC stars in the VVV survey they demonstrated that this peak corresponds with a peak in the stellar density in the region. This would provide an explanation of the dispersion peak within the old and intermediate population as we expect them to be more centrally concentrated.

3.2.2 Latitude Proper Motion

Clarkson et al. (2018) reported gentle trends in latitude proper motions rotation curves but no statistically significant measurement between the near and far sides of the rotation curve. Figure 3.9 presents the latitude proper motion rotation curves of the simulated fields. There are no trends discernible for any of the fields as the amplitude of the proper motion is minimal and the relatively large errors associated greatly reduce the validation of any separation seen.

The dispersion in latitude proper motions is shown in Figure 3.10. The predictions made in Qin et al. (2015) are again measured within all fields. Higher dispersions are seen in the nearest distance bin in comparison to the furthest. Each field also has a peak centred at ≈ 8 kpc. For fields with $|b| = 1^\circ$, the old population

CHAPTER 3

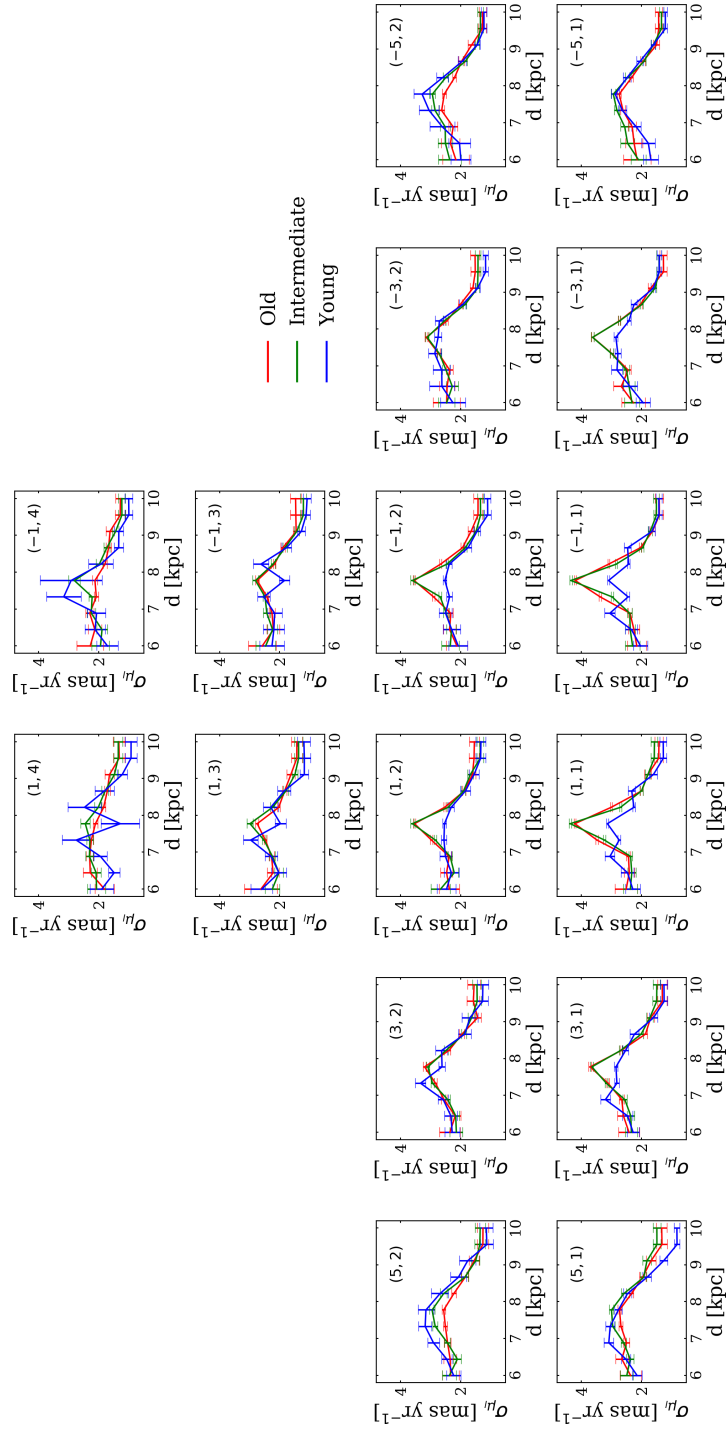


Figure 3.8: The average dispersion in longitudinal proper motion along the line of sight of the simulated fields.

CHAPTER 3

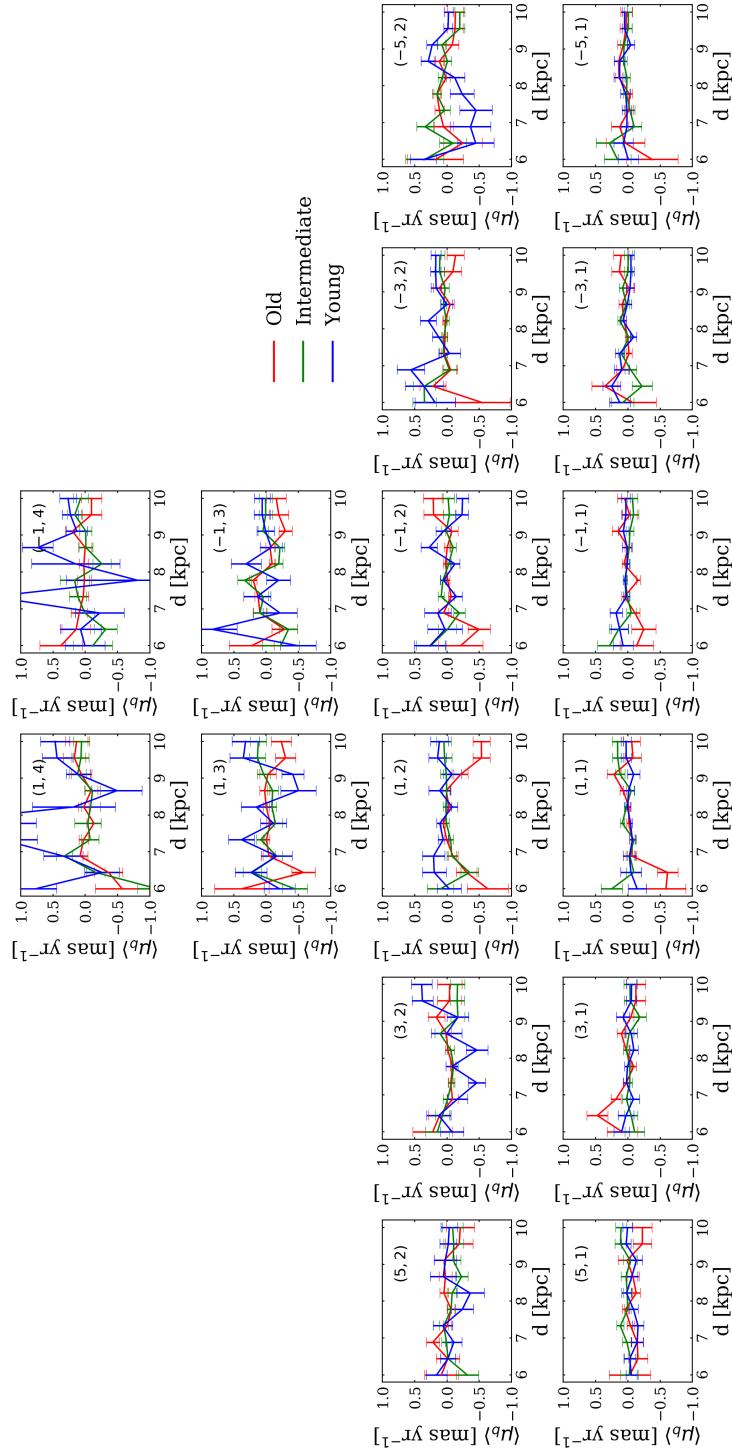


Figure 3.9: The average latitude proper motion rotation curve of the simulated fields.

CHAPTER 3

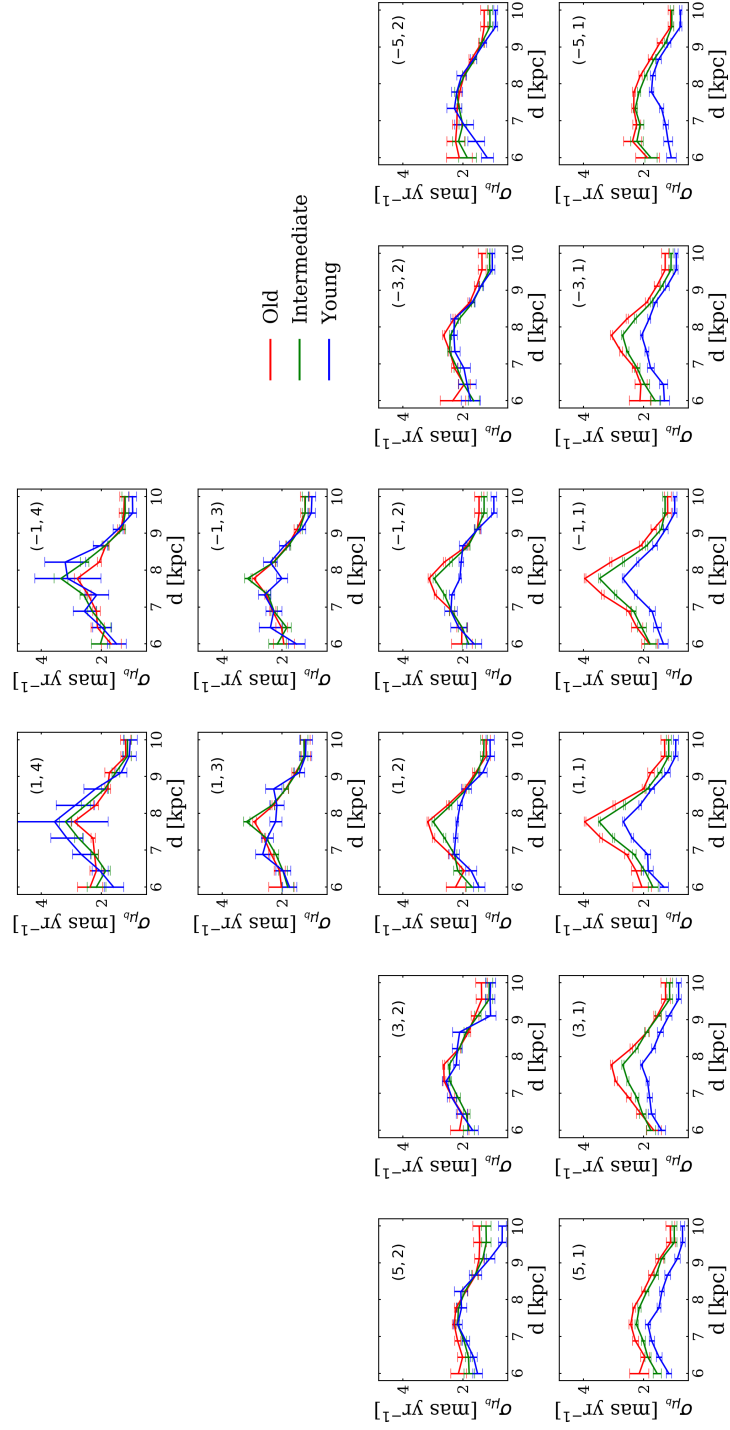


Figure 3.10: The average dispersion in latitude proper motion along the line of sight of the simulated fields.

CHAPTER 3

has the highest dispersions compared the young population with the intermediate tracing between the two. This is also seen in the two central fields at $|b| = 2^\circ$. The rest of the fields do not show significant separation. Similar to the longitudinal proper motion dispersion, the greatest amplitude dispersion in latitude proper motion is seen in the most central fields with the highest density.

3.2.3 Radial Velocity

Exploring the radial velocity rotation curves of the fields (Figure 3.11) the galaxies net rotation is visible within all populations. At longitudes $l > 1$ all populations have positive radial velocity along the line of sight. At longitudes $l < -1$ all populations have negative radial velocity indicating clockwise rotation consistent with previous analysis. These low fields are also expected to be affected by stars on bar orbits due to the bar extending vertically to $\sim 2^\circ$ (Wegg and Gerhard, 2013; Wegg et al., 2015). To determine the extent of this, the bar would have to be isolated. In the central fields the old and intermediate populations show low values of radial velocity, however in every field the young populations have the highest amplitude velocity along the line of sight. This would indicate that the young population rotate faster than the old population. This is suggested by Zoccali et al. (2017) previously mentioned in Chapter 1.

To compare more directly with the data from GIBS, the radial velocities within the Galactic standard rest frame were calculated. This is done with no correction for Solar motion due to two factors. The majority of the Solar velocity correction is tangential to the direction of the Galactic centre so influences the radial velocity minimally close to central longitudes. Secondly this correction will be systematic. As this project attempts to make qualitative comparisons only to the Milky Way, not applying this correction removes the dispute over the values of the Suns velocity. The values were calculated by placing the observer at 8 kpc from the centre of the

CHAPTER 3

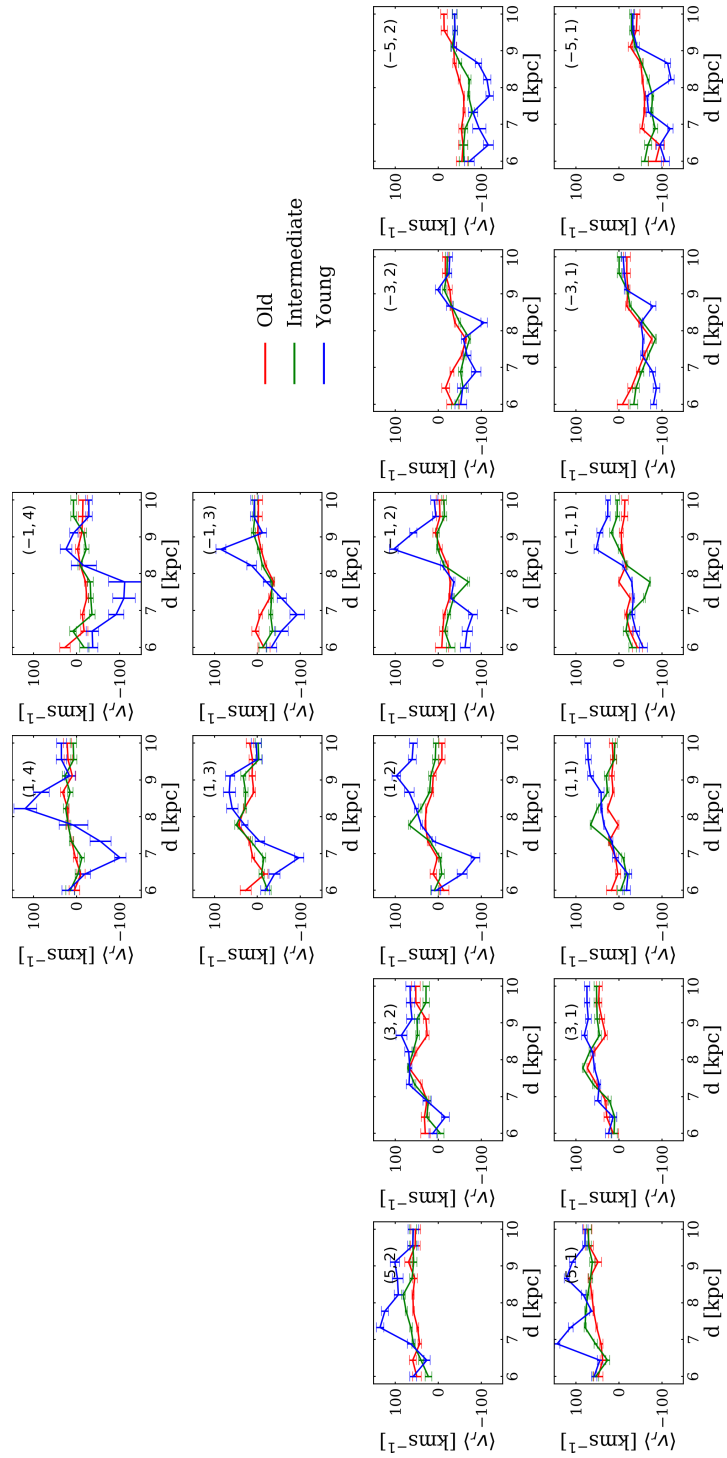


Figure 3.11: The average radial velocity rotation curve of the simulated fields.

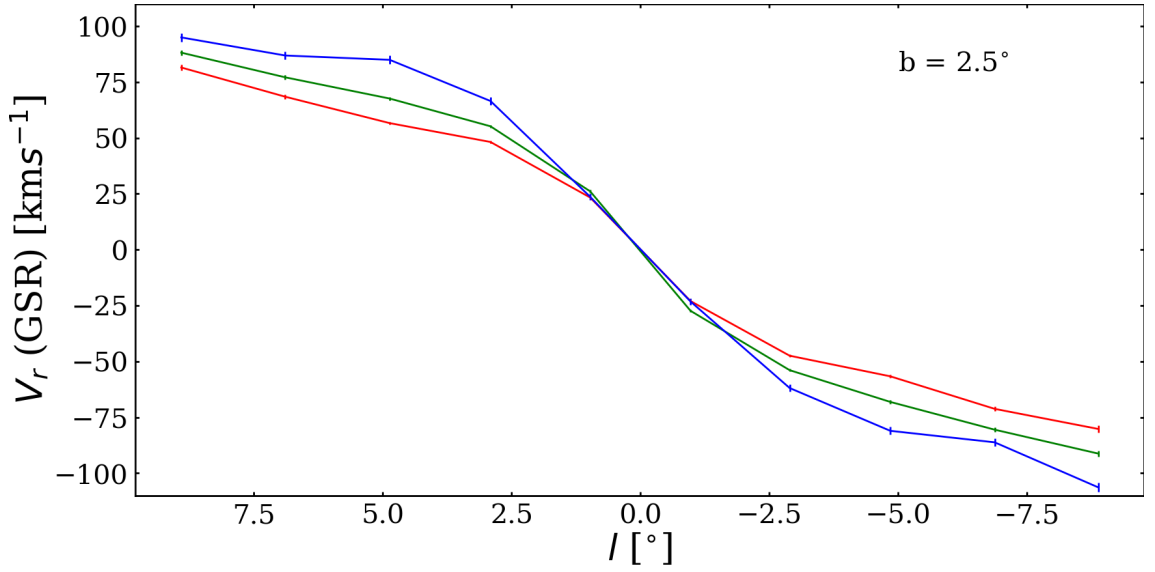


Figure 3.12: The radial velocity against longitude at fixed latitude of $b = 2.5 \pm 0.25^{\circ}$.

simulation.

At fixed latitude $b = 2.5 \pm 0.25^{\circ}$, Figure 3.12, the radial velocity changes from positive to negative with decreasing longitude, crossing 0 km s^{-1} at $l \approx 0^{\circ}$. This agrees with previous measurements of clockwise rotation of the simulation. No difference in gradient through the centre is seen. The amplitude of radial velocity is shown to be largest for the young population with the intermediate population tracing between the young and old. Furthermore, the intermediate population shows separation away from the old beyond $|l| > 2^{\circ}$, reinforcing the interpretation that the small difference in average age between the old and intermediate populations is enough for the signatures of kinematic fraction to be measurable. This would indicate the young population rotates faster within the bulge than the old population. The result which was suggested in the data from Zoccali et al. (2017).

However, when considering same analysis at latitude $b = 5 \pm 0.25^{\circ}$, Figure 3.13, the separation of the populations is not visible. Instead of an curved s-shape through the centre, the distribution is linear. One explanation for not observing these higher trends is the more limited evolution of this simulation in producing a strong X-shape.

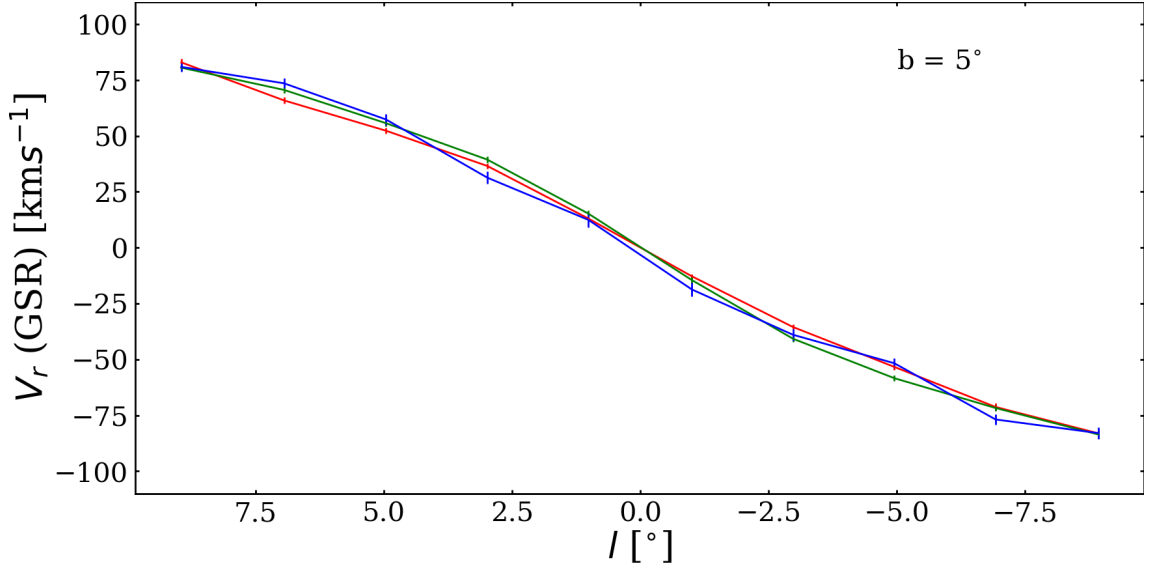


Figure 3.13: The radial velocity against longitude at fixed latitude of $b = 5 \pm 0.25^\circ$.

However, the detection within the observational data was also weak demonstrating that this may not be the best approach to detect kinematic separations within different populations.

The radial velocity dispersion, shown in Figure 3.14, is qualitatively similar to the dispersions of the proper motions. In each field the old population exhibits the highest amount of dispersion with the peak at all ages being centred at ≈ 8 kpc. The expected trend of higher dispersion in the closest bin compared to the furthest was observed again. The largest dispersions were found in the lowest central fields. This is unlike the results of Zoccali et al. (2017) which found metal-rich (young) stars to have higher Galactocentric radial velocity dispersions at the lowest latitude fields.

3.2.4 Age Dissection of Simulated Field

To investigate whether a constraint for the separation of kinematics between differently aged populations a high-density simulated field was dissected further. The field centred on $(l, b) = (1^\circ, 2^\circ)$ is shown in Table 3.1 to have a high-density of stars

CHAPTER 3

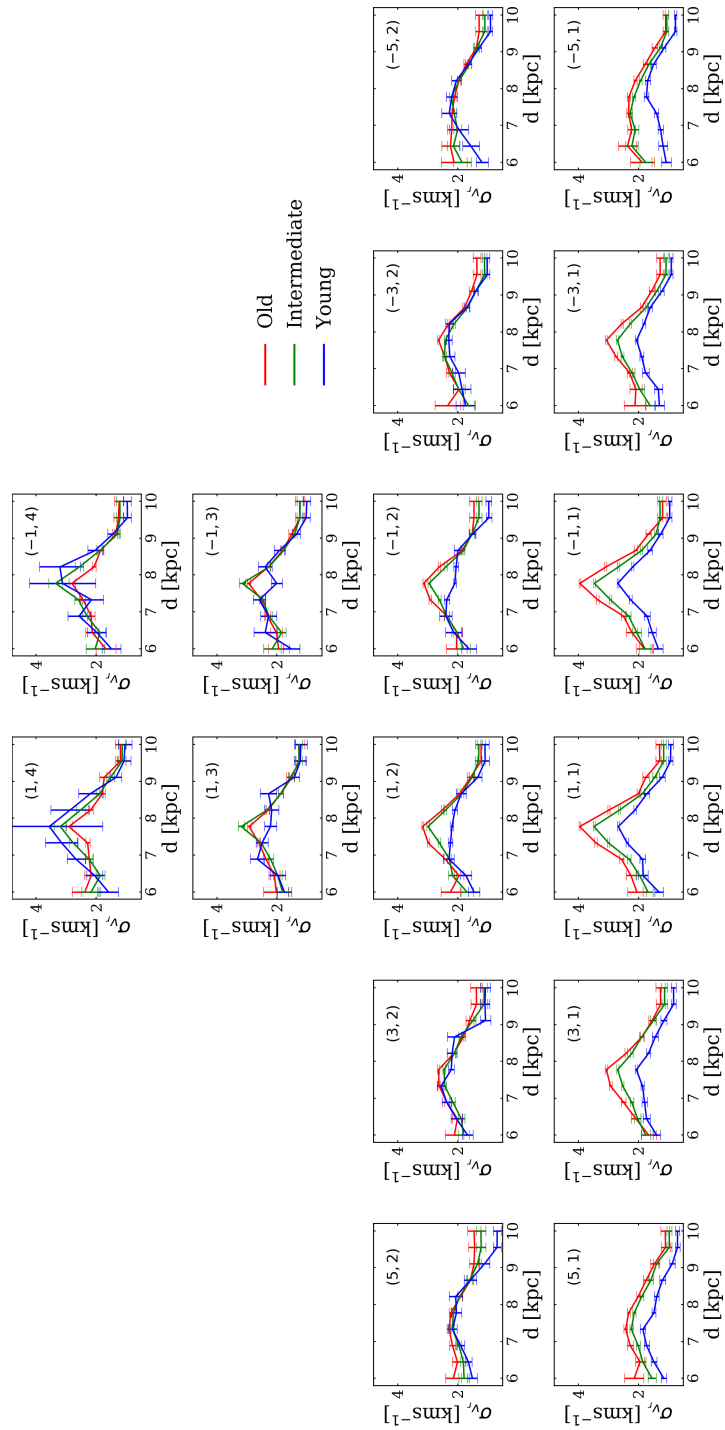


Figure 3.14: The average dispersion in radial velocity along the line of sight of the simulated fields.

CHAPTER 3

in all 3 populations. This field was split not into 3 age populations but by 1 Gyr bins with the exception of stars aged 0 – 4 Gyr. This age range has only a total of 179 collectively stars and could not be split further so was left as one population. The field separated by age is shown in Figure 3.15. Binning in this way, the expected trends from the previous analysis above can still be observed. The youngest two bins (0 – 4 Gyr and 4 – 5 Gyr) have greater amplitude proper motions in comparison to the oldest bin (9 – 10 Gyr) of over a factor of 2 in the nearest distance bins. The stars older than 6 Gyr show minimal separation kinematically except in the very closest bin. However, stars within the 4 – 5 Gyr and 5 – 6 Gyr bins appears to be where the separation begins to be detectable. After 5 Gyr of evolution the simulation already contains a bar which formed at $t \sim 3.2$ Gyr and is beginning to peak in strength. Bar strength is shown to increase the vertical distribution and average radial velocity dispersion of a stellar population in Debattista et al. (2017). This would also imply that correlations of kinematics (like proper motion) will also be imprinted on the populations forming during that period. The detection of this constraint in observational data is more limited due to the levels of error associated with age estimates. During this period at 5 Gyr, gas inflows driven by the bars increasing strength increases star formation within the region and begins to build a nuclear disc within the simulation which later forms 6 Gyr into the simulation. This constraint can only hold true for this simulation however. As this simulation is only evolved for 10 Gyr, it is challenging to compare direct ages.

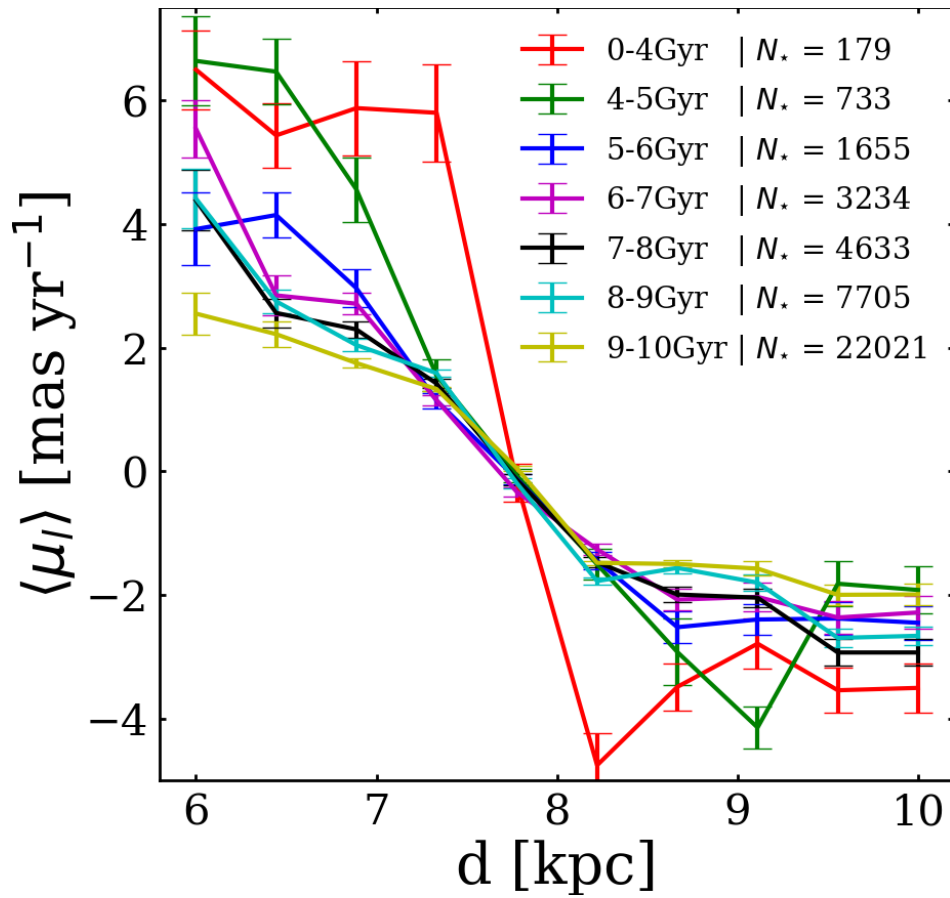


Figure 3.15: Longitudinal proper motion rotation curve of the simulated field centred on $(l, b) = (+1^\circ, +2^\circ)$ separated by stellar age.

Chapter 4

Velocity Maps of the Galactic Bulge

4.1 Current Observational Surveys

Over the past decade advancements in survey data has allowed for an in-depth and large scope investigation into the Galactic centre. The VVV survey covers the majority of the central $10^\circ \times 10^\circ$ of the Milky Way bulge. The survey extends to include the disc but has provided a wealth of data on the bulge to study. The Gaia ESO survey is an all sky investigation into the stars within our galaxy aiming to gather high precision positional, kinematic and chemical data on 1 billion stars. Both surveys have more than one epoch of measurement allowing for the determination of parameters such as proper motions. This gives us A unique view into how kinematics varies across the Galactic surface on a large scale.

The variance of proper motion across the entire central bulge of the simulation was explored by averaging along the line of sight within the distance limits imposed in the previous chapter of 6 kpc to 10 kpc. The bulge was defined within the limits of $|l| < 20^\circ$ and $|b| < 20^\circ$ with 20×20 bins. This give each bin a size of $2^\circ \times 2^\circ$. A

CHAPTER 4

minimum cut was applied to each bin of $N_{\star} > 30$ stars. The field extends beyond the field of the VVV survey and most inner bulge studies to allow for qualitative comparisons to current data and to be able to make predictions to inform further work.

As with the rotation curves, the field was split into 3 populations with the age cuts at 6.5 Gyr and 9 Gyr producing a young, intermediate and old population. The preliminary analysis which was conducted was an examination of the density distribution of each population. Figure 4.1 shows that the young population is not as vertically extended as the old population. A clear X-shaped distribution is only seen in the young population with a slight skew to positive longitude due to the perspective effect of the bars inclined angle to the line of sight. The old population exhibits the rounded distribution of a more 'classical' bulge with the intermediate population appearing marginally more boxy.

These findings are consistent with measurements made by Wegg and Gerhard (2013) showed a asymmetric positive longitude weighted distribution of RC stars from the VVV survey extending to approximately 10° in longitude and latitude.

To be able to directly compare with observational studies the kinematic nature of the centre of the simulation was studied with no cuts on age. In Figure 4.2 the average proper motion in longitude, latitude and the dispersion in each component is presented. For each, the simulation is compared to the published results of Clarke et al. (2019), namely figure 10 of that paper. Their research made use of the data from the VVV Infrared Astrometric Catalogue (VIRAC), Gaia DR2 and a made-to-measure model of the Milky Way. The VIRAC data has measurements of parallax and proper motions of 119 million stars. Combined with Gaia for the refinement and incorporation of a well-defined absolute reference frame provides a high-resolution view of the Galactic centre down to low latitudes. Two points of clarification are that for some panels in Clarke et al. (2019) have an inverted colour scale and they

CHAPTER 4

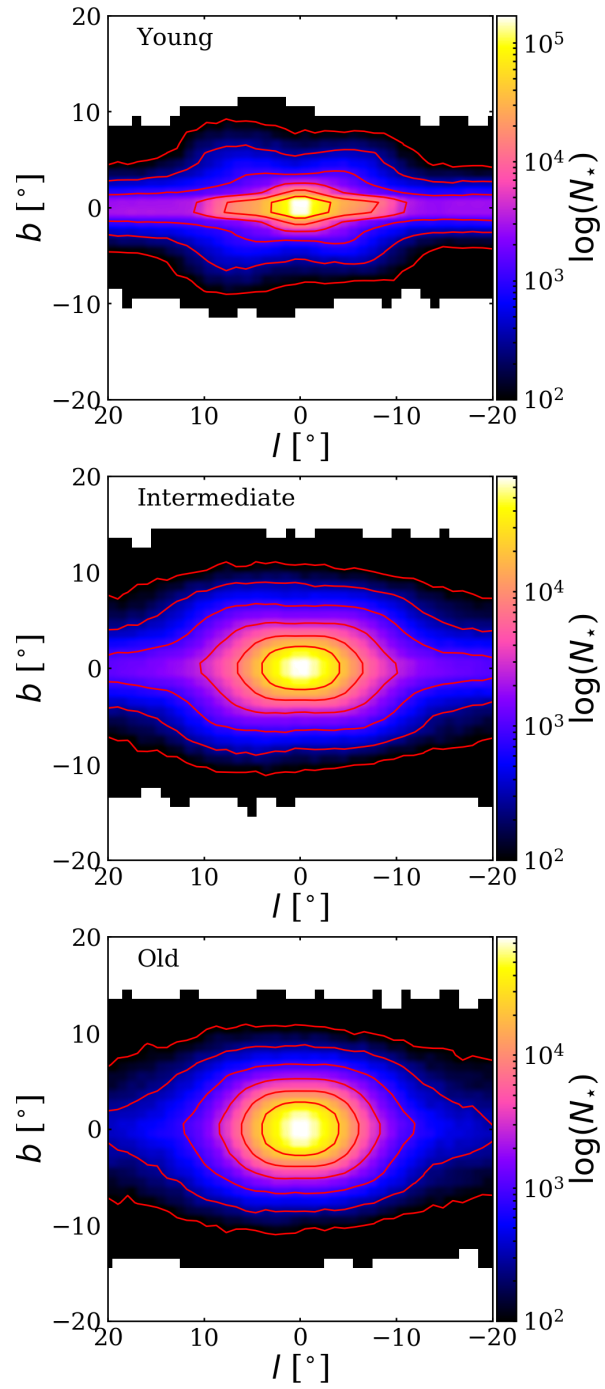


Figure 4.1: X-Y density map of the central bulge for each population.

CHAPTER 4

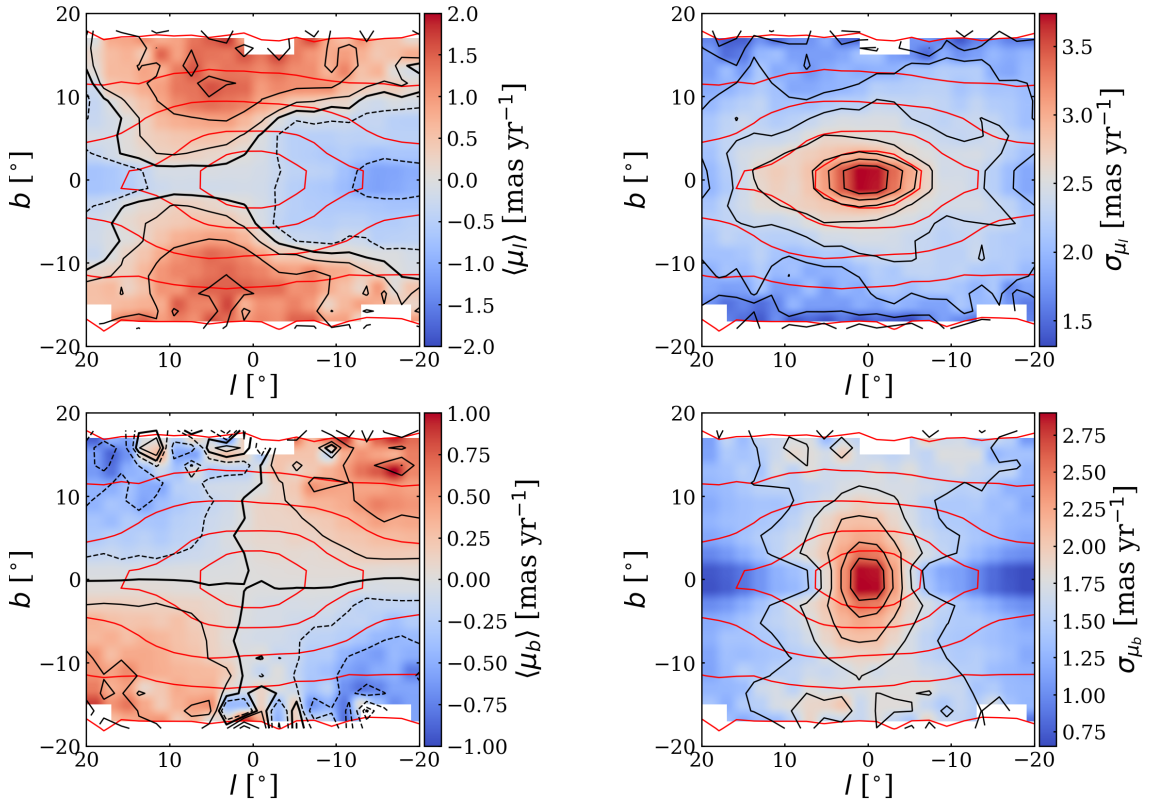


Figure 4.2: Maps of the proper motions and dispersions of the central bulge for all ages. Longitude proper motion (top left), dispersion of longitude proper motion (top right), latitude proper motion (bottom left) and dispersion in latitude proper motion (bottom right)

present their results in the heliocentric rest frame. The dispersions in proper motions can also be compared to a study by Sanders et al. (2019) who made similar use of the VIRAC data and Gaia DR2.

To add context to the signatures of structures within the bulge, consider the bar length of this projects simulation to be 3.6 kpc at an inclined angle of 27° . The end of the bar on the near side will extend to $l \sim 12^\circ$ longitude and on the far side to $l \sim -5^\circ$. A kiloparsec nuclear disc would extend to $l \sim \pm 7^\circ$ and both structures have a small vertical height so remain part of the plane. however, the X-shaped distribution can potentially be measured at heights of $b \approx \pm 10^\circ$

4.2 Proper Motion Maps

The longitudinal proper motion is seen to have a vertical gradient increasing in amplitude with increasing latitude. Larger amplitude proper motion is seen centred at $(l, b) = (5^\circ, \pm 10^\circ)$ which is potentially the of the X-shape on the near side. The most negative proper motions are found in the plane at large longitudes. These panel matches the results found in Clarke et al. (2019) who suggest the asymmetry from left to right is due to the B/P shape of the bar.

Proper motions in latitude show a clear quadrupole distribution. At positive longitude the motion suggests the stars are pinching vertically and at negative longitude the stars appear to be separating. This is a manifestation of the clockwise rotation of the galaxy. Stars above the plane moving away appear to move lower and stars moving closer appear to move higher in a perspective view which is not seen in an orthographic view of vertical heights. Amplitude of latitude proper motion increases as you move to higher latitudes and longitudes as expected by this effect. Observations of latitude proper motion are reported to be more of a shifted quadrupole distribution. Being only shifted by a few degrees due to the bars presence the resolution of the maps from the simulation is not enough to reproduce this.

The dispersion in longitudinal proper motion has an asymmetry towards positive proper motion and is concentrated towards the centre decreasing radially outwards. The decrease in dispersion is more rapid moving toward negative longitude than positive longitude. This is most likely due to the bars inclination angle matched very closely by observation. The dispersion in latitude proper motion shows a more pinched distribution with dispersion remaining higher at central longitudes with increasing latitude. Moving away from the centre along the plane the dispersion drops significantly. This is consistent with a rotation perspective effect. Clarke et al. (2019) show a slight asymmetry in the dispersion within the central 5° however our

CHAPTER 4

resolution does not replicate this.

To reveal more about which population contributes most to the features seen in the combined field, the proper motions and dispersions were separated into the old, intermediate and young populations.

The longitudinal proper motions are displayed in Figure 4.3. Upon first glance it is easy to determine that the population with the regions of large amplitude longitude proper motion is the young population. Regions centred at $(l, b) = (5^\circ, \pm 10^\circ)$ show the largest positive longitudinal proper motion. This corresponds to the tip of the X-shape on the near side. At $(l, b) = (-5^\circ, \pm 10^\circ)$ high amplitude negative longitudinal proper motion can be observed peaking at slightly lower latitude in this region. Again, due to the perspective effect we expect to find the tip of the X-shape on the far side at a lower latitude. These regions are not seen in the intermediate and old populations as intense peaks but as lower amplitude diffuse regions. Large positive proper motions are seen at high latitude in all three populations, most likely due to the perspective effect of observing lower vertical heights at the closest distance limit compared the furthest. At 6 kpc from the observers position at 10° latitude corresponds to a vertical height of ≈ 1 kpc. At the furthest distance of 10 kpc, the vertical height observed at the same latitude is ≈ 1.75 kpc. The density this far out the plan is significantly less so contributes less to the line of sight averaged proper motion. The line of sight at these latitudes are dominated by close stars moving towards positive longitudes with the rotation of the galaxy. Close to the plane the average longitudinal proper motions of each population are close to zero decreasing to negative values away from the galactic centre.

Figure 4.4 presents the latitude proper motions for each of the populations. A quadrupole morphology can be seen at all ages in, Figure 4.2, with similar gradients radially from the centre. This indicates that the trends seen are a feature of perspective and not a physical feature of the stars themselves. A slight asymmetry can

CHAPTER 4

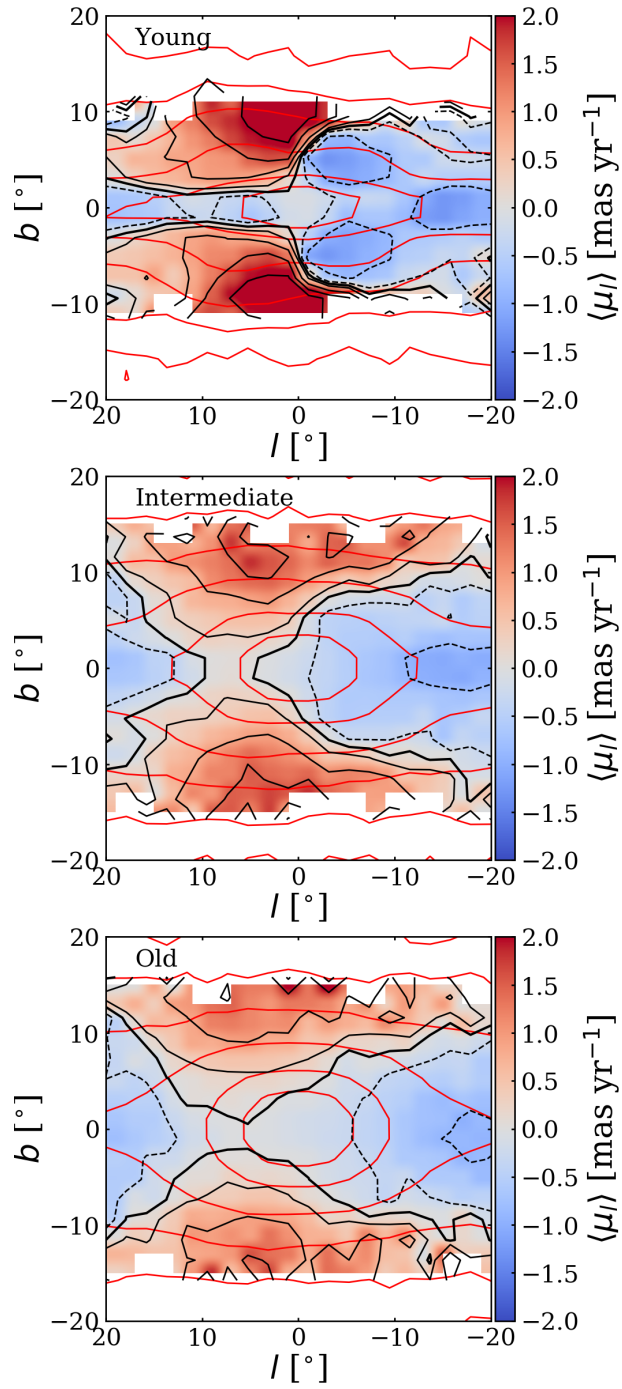


Figure 4.3: Maps of the average longitude proper motions of the three populations.

CHAPTER 4

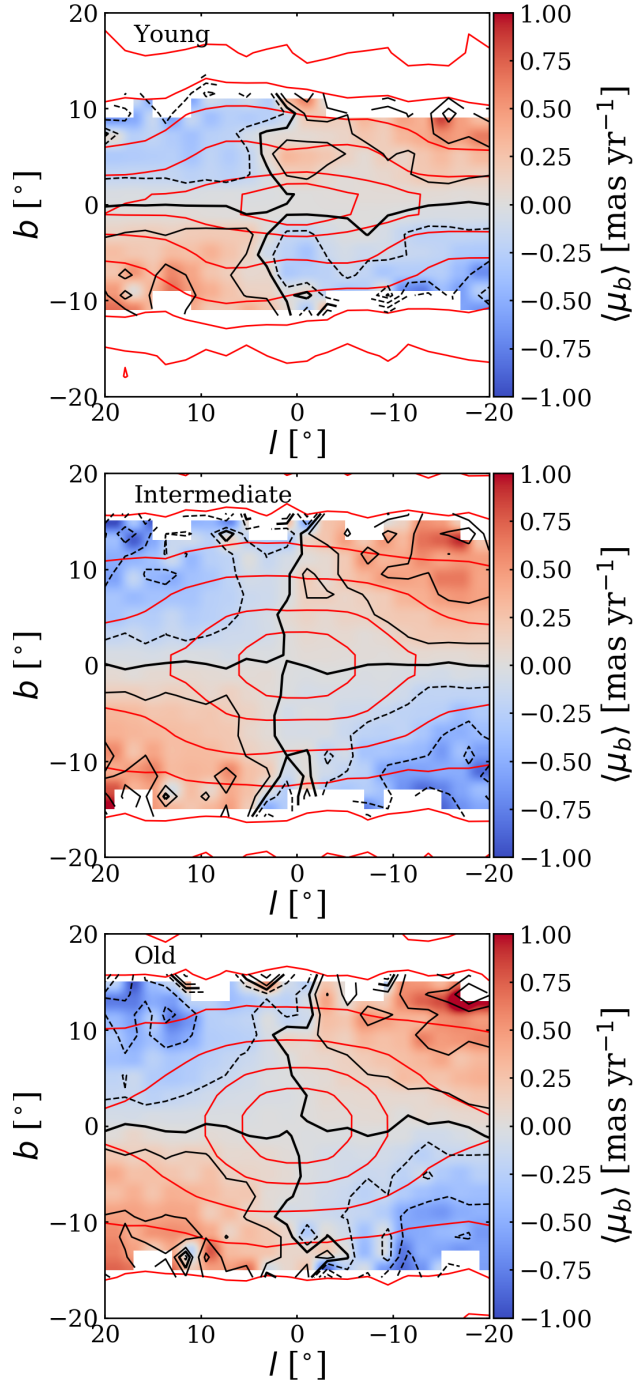


Figure 4.4: Maps of the average latitude proper motions of the three populations.

CHAPTER 4

be seen in the youngest population. The largest amplitude latitude proper motion is seen in the old population, but this is due to it having the greatest extent out of the plane. The density of the young stars drops at high latitude.

In Figure 4.5 the dispersion of longitude proper motion was explored within the galactic centre. The young population has the largest central dispersions and demonstrates the greatest asymmetry. At high latitudes the dispersion in the young population decreases to minimal values creating a steep vertical gradient. The intermediate and old populations have a less steep vertical gradient. All populations show an asymmetry towards positive latitude with the largest being the young population. This is most likely due to this population more closely tracing the bar and forming a strong B/P shape. The old population is more spherical but is asymmetric due to the inclined bar angle.

The dispersion in latitude proper motion is shown in Figure 4.6. The greatest dispersion is found in the old population which extended vertically creating a steady decrease in dispersion with increasing latitude. Dispersion decreases more rapidly moving from the centre outwards along the plane in all populations. The young population shows the greatest decrease in dispersion as it has a highly pinched distribution. The two lobes above and below the plane reflect the peanut shaped region of the inner bulge most closely traced by the young population. Its asymmetry again arises from the bar. The intermediate age population shows slight pinching but remains more cylindrical similar to the old population. If the distribution of dispersion in the old population was pinched, it could be assumed that was purely a rotation perspective effect. However, its cylindrical shape may indicate that secular evolution is still ongoing for this simulation.

Figure 4.7 shows the dispersion ratio, $\sigma_{\mu_l}/\sigma_{\mu_b}$ of the central bulge. The largest dispersion ratio is seen in the youngest population along the plane excluding the central few degrees. Above the plane a peanut shaped distribution can be seen

CHAPTER 4

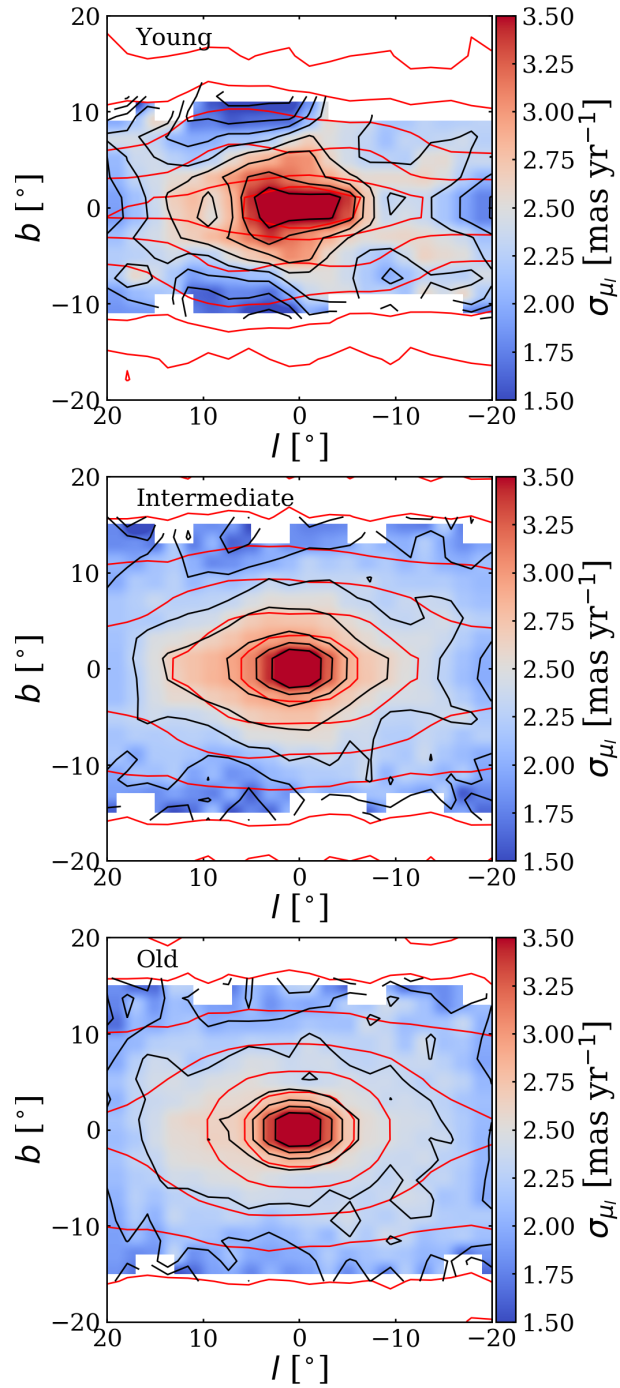


Figure 4.5: Maps of the average dispersion longitude proper motions of the three populations.

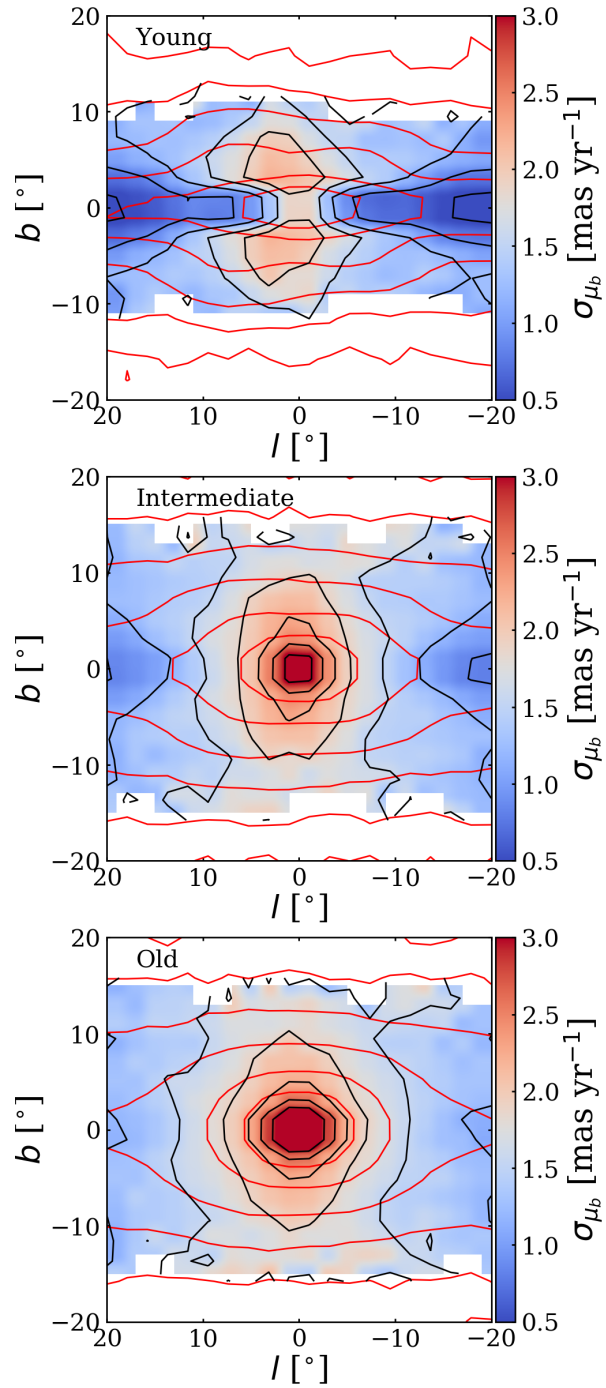


Figure 4.6: Maps of the average dispersion latitude proper motions of the three populations.

CHAPTER 4

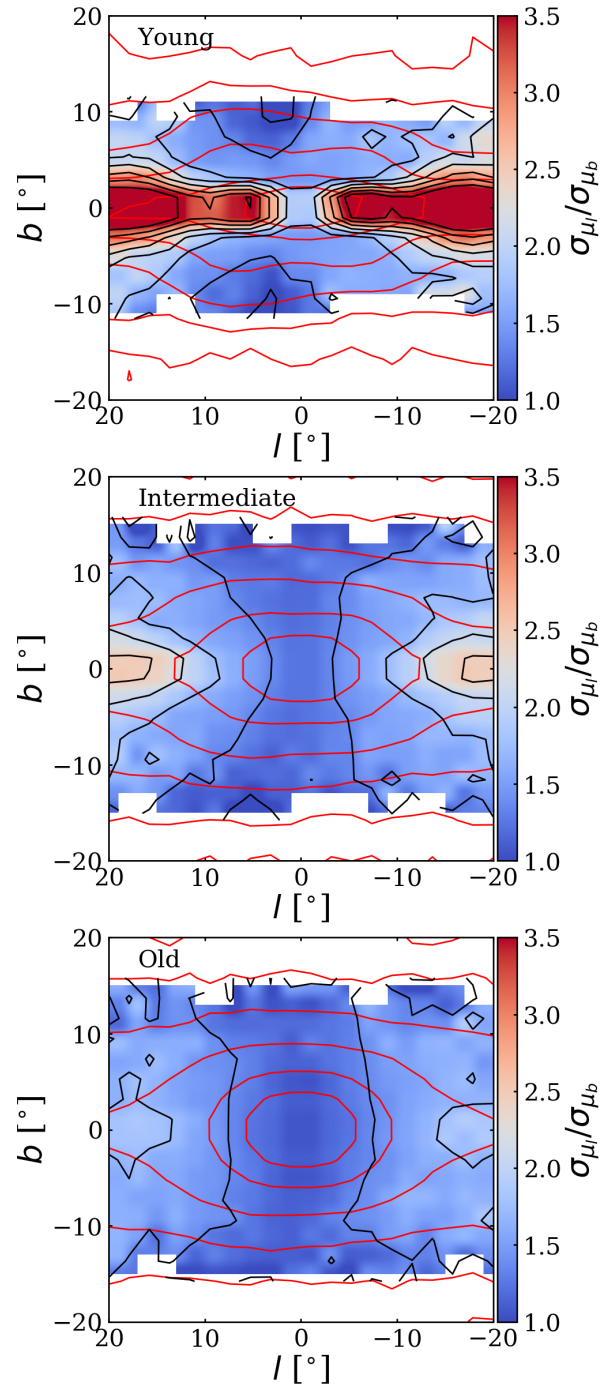


Figure 4.7: Maps of the average ratio of longitude proper motion dispersion to latitude proper motions proper motions of the three populations.

CHAPTER 4

with a slight asymmetry to positive longitude and a minimum value at $(l, b) = (5^\circ, \pm 10^\circ)$. In the intermediate population the dispersion ratio shows slight pinching and asymmetry towards positive longitude. This population shows more pinching at positive longitude than negative showing that the weak trends are caused by the bar. The old population show uniform and low values of dispersion ratio, indicating the dispersion ratio traces the X-shape of the Milky Way bulge. Observational data from both Clarke et al. (2019) and Sanders et al. (2019) which show a broadened but pinched distribution in agreement with the results presented. This would imply that the main contributor to the observed distribution is the young stars.

4.3 Velocity Correlations

The correlations of longitudinal proper motion and latitude proper motion (Figure 4.8) show a clear quadrupole structure, similar to distribution of latitude proper motion. Low correlations are found at values of $b = 0^\circ$ and $l = 0^\circ$ increasing outwards. For all populations, positive longitudes have higher correlations than negative. This is interpreted as a consequence of the viewing angle of the bar. The correlations are greatest in the young population close to the vicinity of the end of the bar most likely due to this population forming a stronger bar. The same structure is seen in both observational studies. Their observed correlations have lower values on average, however, this is to be expected with the increase of observational error and scatter.

CHAPTER 4

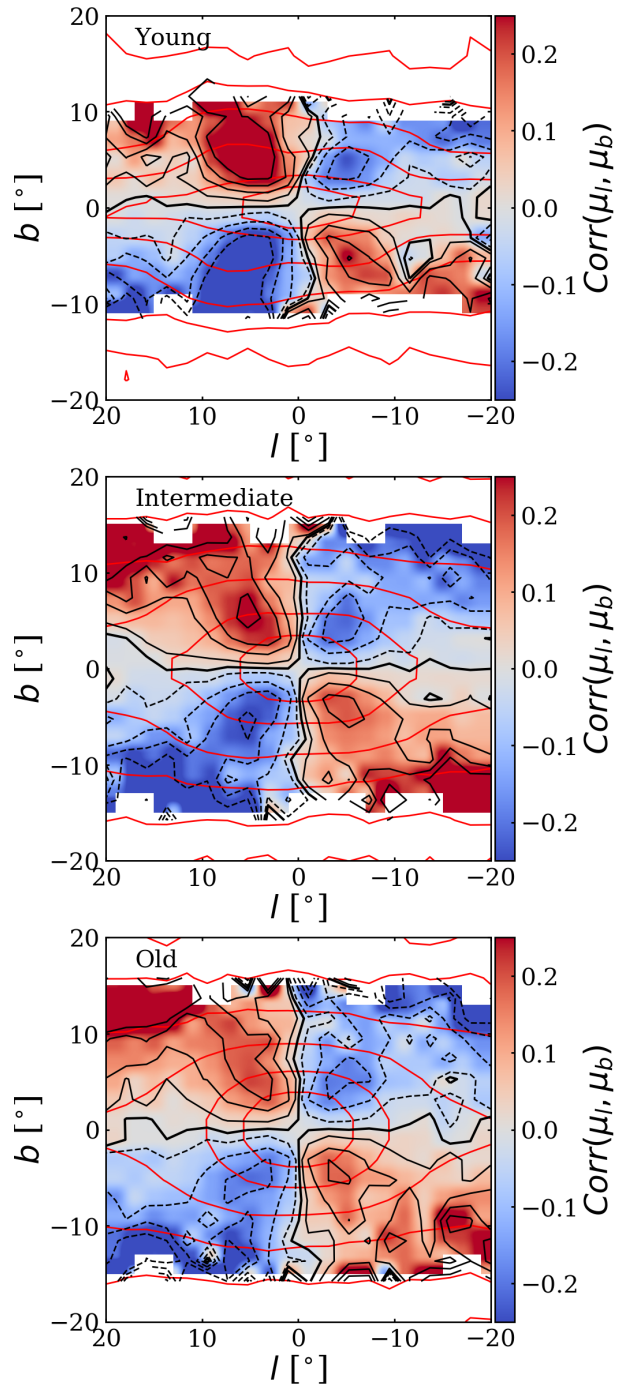


Figure 4.8: Maps of the average correlation of longitude proper motion to latitude proper motions proper motions of the three populations.

Chapter 5

Conclusions

This project has aimed to reproduce the observed kinematic separation of metal-rich and metal-poor stars within the Galactic bulge using an N-body+SPH simulation. The simulation has a bar with length of 3.6 kpc and hosts a kiloparsec nuclear disc (Ness et al., 2014; Cole et al., 2014). During its evolution in isolation the simulation goes through kinematic fractionation resulting in a B/P shaped distribution with signatures of an X-shaped structure (Debattista et al., 2017). The correlation between age and metallicity is discussed in the introductory chapters with the association of young stars with metal-rich stars and old stars with metal-poor stars. The SWEEPS field explored by Clarkson et al. (2018) is replicated within the simulation. The simulation produced qualitatively similar separation in the longitudinal proper motions of old and young stars, matching the separation of metal-rich and metal-poor stars observed in the Milky-Way. The same process is used to make predictions for three other observational fields which have the potential to conduct a similar study. From simulating those fields, it was determined that observing longitudinal proper motion rotation curves far from the galactic centre ($l > 7^\circ$) results in little to no separation between different age populations. Therefore, a field such as OGLE29 would show significantly less separation in proper motion of metal-rich and metal-poor stars along the line of sight, if any at all.

CHAPTER 5

With these basic predictions of the Galactic centre, the analysis was expanded to cover an array of fields across the centre of the simulated galaxy. In longitudinal proper motion we see qualitatively similar trends across most fields which decline with observations at increasing longitude in both directions. In latitude proper motions we find no trends in any of the fields. This suggests the weak trends found by Clarkson et al. (2018) may be a small-scale trend not reproducible by this simulation or may be unique to this window of observation and will not be seen in other Milky Way fields. The dispersions of both proper motions match what is expected from the spatial distribution of the stellar populations as well as perspective effects of viewing in spherical coordinates (Qin et al., 2015). Considering the radial velocities along the line of sight revealed that the young population is rotating faster than the old population, in agreement with observational studies (Zoccali et al., 2017). By dissecting a high-density field into small age bins, a constraint on measuring the separation of longitude proper motion was determined. It suggested that separations begin to show roughly ~ 2 Gyr after the formation of the bar and during a period of major strengthening of the bar.

As well as being able to match rotation curves to high-density observational fields, simulated maps of the galactic centre were compared to surveys conducted within the bulge. Observations of this nature have larger scale smoothing that makes it difficult to directly compare small scale differences but qualitative general trends are reproduced in each component of proper motion and their dispersions. Asymmetries are more prevalent when considering the bulge beyond the central 5° . These are an artefact of the bar's inclined angle (27° within the simulation) which further reinforces the presence of a bar within the Milky Way. Within the kinematic maps of the galactic centre, the signatures of X-shaped and peanut distributions are seen both in simulation and observations (Clarke et al., 2019; Sanders et al., 2019).

Separating the stellar populations by age, it is clear that the young populations

CHAPTER 5

trace the bar and structures within the bulge more closely. This is in line with predictions made by Debattista et al. (2017) regarding the internal evolution of the bulge. Although the Milky Way did not form in isolation, resulting in several tidal streams and accreted populations, this project heavily suggests that the Galaxy went through the process of kinematic fractionation within its bulge during its evolution. Most likely the Milky Way contains a compound bulge which demonstrates a B/P component built by kinematic fractionation and a spherical component from its formation and merging events.

The qualitative reproduction of kinematic maps presents further evidence of the Milky Way hosting a bar in its centre which drove the evolution of a B/P bulge. The differences in morphology and kinematics between old and young stars within the simulation suggest that the evolution of this bulge followed the process of kinematic fractionation. It is interpreted that kinematic fractionation can embed kinematic trends in the chemistry of bulge stars such as proper motions and dispersions.

To progress this project and its analysis, the study of different simulations may reveal further insights and be a more direct comparison to the Milky Way. The cosmological simulation of Debattista et al. (2019) from the FIRE project is shown to exhibit a B/P bulge. It contains merging and accretion events along with an AMR with a stronger correlation between age and metallicity. Separating by metallicity to uncover differences in longitude proper motion may be possible here. The simulation in this project is helpful for determining the pure contribution of internal evolution, however, being able to compare this contribution to external influence will be more applicable. The measurements of a simulation with no B/P bulge component will augment the measurements similar to the previous statement. The kinematics of a spherical bulge can be subtracted from a compound bulge to leave only the B/P component which may emphasise its features.

This project was conducted with the simulation evolved to 10 Gyr to make a

CHAPTER 5

comparison to observations. To further reinforce the theoretical considerations, analysing how the proper motions change through the evolution of the simulation could potentially add insights into the history and projected changes of the simulation and the Milky Way. This can be achieved by analysing multiple snapshots of the simulation.

Further prospects await the release of Gaia DR3 and the expanded VVV survey (**VVVx**) will provide higher resolution measurements covering a wider field than what is presently available. This along with new surveys such as the Large Synoptic Survey Telescope (**LSST**) which will add more measurements to the mapping of the Galaxy and its bulge. The launch of the James Webb Space Telescope (**JWST**) will explore the early universe and give insights into the early formation history of external galaxies. These observations will expose processes such as buckling in these early galaxies and give indications as to how the Milky Way has evolved through its formation.

Bibliography

- Abbott, C., Valluri, M., Shen, J., and Debattista, V. P. (2017). On the orbits that generate the X-shape in the Milky Way bulge. *Monthly Notices of the Royal Astronomical Society*, 470(2):1526–1541.
- Athanassoula, E. (2005). On the nature of bulges in general and of box/peanut bulges in particular: input from N-body simulations. *Monthly Notices of the Royal Astronomical Society*, 358(4):1477–1488.
- Bekki, K. and Tsujimoto, T. (2012). Chemical Evolution of the Large Magellanic Cloud. *The Astrophysical Journal, Volume 761, Issue 2, article id. 180, 19 pp. (2012).*, 761.
- Binney, J., Gerhard, O., and Spergel, D. (1996). The photometric structure of the inner Galaxy. *Monthly Notices of the Royal Astronomical Society, Volume 288, Issue 2, pp. 365-374.*, 288:365–374.
- Binney, J., Gerhard, O. E., Stark, A. A., Bally, J., and Uchida, K. I. (1991). Understanding the kinematics of Galactic Centre gas. *Monthly Notices of the Royal Astronomical Society*, 252(2):210–218.
- Binney, J. and Tremaine, S. (2008). *Galactic dynamics*. Princeton University Press.
- Bovy, J. and Jo (2014). galpy: A Python Library for Galactic Dynamics. *The*

- Astrophysical Journal Supplement Series, Volume 216, Issue 2, article id. 29, 27 pp. (2015).*, 216.
- Calamida, A., Sahu, K. C., Anderson, J., Casertano, S., Cassisi, S., Salaris, M., Brown, T., Sokol, J., Bond, H. E., Ferraro, I., Ferguson, H., Livio, M., Valenti, J., Buonanno, R., Clarkson, W., and Pietrinferni, A. (2014). First Detection of the White-Dwarf Cooling Sequence of the Galactic Bulge. *The Astrophysical Journal, Volume 790, Issue 2, article id. 164, 7 pp. (2014).*, 790.
- Carollo, C. M., Stiavelli, M., and Mack, J. (1998). Spiral Galaxies with WFPC2. II. The Nuclear Properties of 40 Objects. *The Astronomical Journal*, 116(1):68–84.
- Chang, C.-K., Ko, C.-M., and Peng, T.-H. (2011). The Information Of The Milky Way From 2MASS Whole Sky Star Count: The Structure Parameters. *The Astrophysical Journal, Volume 740, Issue 1, article id. 34, 8 pp. (2011).*, 740.
- Chiappini, C., Matteucci, F., and Romano, D. (2001). Abundance Gradients and the Formation of the Milky Way. *The Astrophysical Journal*, 554(2):1044–1058.
- Cignoni, M., Cole, A. A., Tosi, M., Gallagher, J. S., Sabbi, E., Anderson, J., Grebel, E. K., and Nota, A. (2013). Mean Age Gradient and Asymmetry in the Star Formation History of the Small Magellanic Cloud. *The Astrophysical Journal, Volume 775, Issue 2, article id. 83, 13 pp. (2013).*, 775.
- Clarke, J. P., Wegg, C., Gerhard, O., Smith, L. C., Lucas, P. W., and Wylie, S. M. (2019). The Milky Way bar/bulge in proper motions: a 3D view from VIRACand Gaia. *Monthly Notices of the Royal Astronomical Society*, 489(3):3519–3538.
- Clarkson, W., Sahu, K., Anderson, J., Smith, E., Brown, T. R., Casertano, S., Rich, R., Bond, H. E., Livio, M., Minniti, D., Panagia, N., Renzini, A., Valenti, J., and Zoccali, M. (2007). New Stellar Proper Motions in the Galactic Bulge with

- HST. *American Astronomical Society, AAS Meeting #211, id.33.06; Bulletin of the American Astronomical Society, Vol. 39, p.786, 39:786.*
- Clarkson, W. I., Calamida, A., Sahu, K. C., Brown, T. M., Gennaro, M., Avila, R. J., Valenti, J., Debattista, V. P., Rich, R. M., Minniti, D., Zoccali, M., and Aufdenberge, E. R. (2018). Chemically Dissected Rotation Curves of the Galactic Bulge from Main-sequence Proper Motions. *The Astrophysical Journal*, 858(1):46.
- Cole, D. R., Debattista, V. P., Erwin, P., Earp, S. W. F., and Roskar, R. (2014). The formation of stellar nuclear discs in bar-induced gas inflows. *Monthly Notices of the Royal Astronomical Society*, 445:3352–3369.
- de Vaucouleurs, G. H., de Vaucouleurs, A., and Shapley, H. (1964). Reference catalogue of bright galaxies. *University of Texas Monographs in Astronomy, Austin: University of Texas Press, —c1964.*
- Debattista, V. P., Gonzalez, O. A., Sanderson, R. E., El-Badry, K., Garrison-Kimmel, S., Wetzel, A., Faucher-Giguère, C.-A., and Hopkins, P. F. (2019). Formation, vertex deviation, and age of the Milky Way’s bulge: input from a cosmological simulation with a late-forming bar. *Monthly Notices of the Royal Astronomical Society*, 485(4):5073–5085.
- Debattista, V. P., Mayer, L., Carollo, C. M., Moore, B., Wadsley, J., and Quinn, T. (2006). The Secular Evolution of Disk Structural Parameters. *The Astrophysical Journal, Volume 645, Issue 1, pp. 209-227.*, 645:209–227.
- Debattista, V. P., Ness, M., Earp, S. W. F., and Cole, D. R. (2015). A Kiloparsec-Scale Nuclear Stellar Disk in the Milky Way as a Possible Explanation of the High Velocity Peaks in the Galactic Bulge. *The Astrophysical Journal Letters*, 812:L16.
- Debattista, V. P., Ness, M., Gonzalez, O. A., Freeman, K., Zoccali, M., and Minniti, D. (2017). Separation of Stellar Populations by an Evolving Bar: Implications for

- the Bulge of the Milky Way. *Monthly Notices of the Royal Astronomical Society*, 469(2):1587–1611.
- Debattista, V. P. and Sellwood, J. A. (2000). Constraints from Dynamical Friction on the Dark Matter Content of Barred Galaxies. *The Astrophysical Journal*, Volume 543, Issue 2, pp. 704-721., 543:704–721.
- Erwin, P. and Debattista, V. P. (2016). Caught in the Act: Direct Detection of Galactic Bars in the Buckling Phase. *The Astrophysical Journal Letters*, Volume 825, Issue 2, article id. L30, 6 pp. (2016)., 825.
- Erwin, P. and Debattista, V. P. (2017). The Frequency and Stellar-Mass Dependence of Boxy/Peanut-Shaped Bulges in Barred Galaxies. *Monthly Notices of the Royal Astronomical Society*, Volume 468, Issue 2, p.2058-2080, 468:2058–2080.
- Eskridge, P. B., Frogel, J. A., Pogge, R. W., Quillen, A. C., Davies, R. L., DePoy, D. L., Houdashelt, M. L., Kuchinski, L. E., Ramírez, S. V., Sellgren, K., Terndrup, D. M., and Tiede, G. P. (2000). The Frequency of Barred Spiral Galaxies in the Near-Infrared. *The Astronomical Journal*, 119(2):536–544.
- Fukugita, M., Hogan, C. J., and Peebles, P. J. E. (1998). The Cosmic Baryon Budget. *The Astrophysical Journal*, Volume 503, Issue 2, pp. 518-530., 503:518–530.
- Fux, R. and R. (1997). 3D self-consistent N-body barred models of the Milky Way: I. Stellar dynamics. *Astronomy and Astrophysics*, v.327, p.983-1003 (1997), 327:983–1003.
- Fux, R. and R. (1999). 3D self-consistent N-body barred models of the Milky Way: II. Gas dynamics. *Astronomy and Astrophysics*, v.345, p.787-812 (1999), 345:787–812.
- Gardner, E., Debattista, V. P., Robin, A. C., Vásquez, S., and Zoccali, M. (2013). N-body simulation insights into the X-shaped bulge of the Milky Way: Kinematics

- and distance to the Galactic Centre. *Monthly Notices of the Royal Astronomical Society*, Volume 438, Issue 4, p.3275-3290, 438:3275–3290.
- Gerhard, O. E. and Vietri, M. (1986). The peculiar shape of the inner galactic rotation curve. *Monthly Notices of the Royal Astronomical Society*, 223(2):377–389.
- Gibson, B. K., Fenner, Y., Renda, A., Kawata, D., and Lee, H.-c. (2003). Galactic Chemical Evolution. *Publications of the Astronomical Society of Australia*, 20(4):401–415.
- Gillessen, S., Eisenhauer, F., Trippe, S., Alexander, T., Genzel, R., Martins, F., and Ott, T. (2008). Monitoring stellar orbits around the Massive Black Hole in the Galactic Center. *The Astrophysical Journal*, Volume 692, Issue 2, pp. 1075-1109 (2009)., 692:1075–1109.
- Girardi, L. (1999). A secondary clump of red giant stars: why and where. *Monthly Notices of the Royal Astronomical Society*, 308(3):818–832.
- Girardi, L. and Salaris, M. (2000). Population effects on the Red Giant Clump absolute magnitude, and distance determinations to nearby galaxies. *Monthly Notices of the Royal Astronomical Society*, Volume 323, Issue 1, pp. 109-129., 323:109–129.
- Gonzalez, O. A., Rejkuba, M., Minniti, D., Zoccali, M., Valenti, E., and Saito, R. K. (2011). The inner Galactic bar traced by the VVV survey. *Astronomy & Astrophysics*, Volume 534, id.L14, 4 pp., 534.
- Gonzalez, O. A., Zoccali, M., Vasquez, S., Hill, V., Rejkuba, M., Valenti, E., Rojas-Arriagada, A., Renzini, A., Babusiaux, C., Minniti, D., and Brown, T. M. (2015).

- The Giraffe Inner Bulge Survey (GIBS) II. Metallicity distributions and alpha element abundances at fixed Galactic latitude. *Astronomy & Astrophysics, Volume 584, id.A46, 11 pp.*, 584.
- Karttunen, H., Kröger, P., Oja, H., Poutanen, M., and Donner, K. J., editors (2017). *Fundamental Astronomy*. Springer Berlin Heidelberg, Berlin, Heidelberg.
- Kormendy, J. and Kennicutt, R. C. (2004). Secular Evolution and the Formation of Pseudobulges in Disk Galaxies. *Annual Review of Astronomy & Astrophysics, vol. 42, Issue 1, pp.603-683*, 42:603–683.
- Kuijken, K. and Rich, R. M. (2002). HST/WFPC2 proper motions in two bulge fields: kinematics and stellar population of the Galactic bulge. *The Astronomical Journal, Volume 124, Issue 4, pp. 2054-2066.*, 124:2054–2066.
- Loebman, S. R., Roskar, R., Debattista, V. P., Ivezić, Z., Quinn, T. R., and Wadsley, J. (2010). The Genesis of the Milky Way’s Thick Disk via Stellar Migration. *The Astrophysical Journal, Volume 737, Issue 1, article id. 8, 17 pp. (2011).*, 737.
- Martinez-Valpuesta, I. and Gerhard, O. (2011). Unifying boxy bulge and planar long bar in the Milky Way. *The Astrophysical Journal Letters, Volume 734, Issue 1, article id. L20, 4 pp. (2011).*, 734.
- McMillan, P. J. and J., P. (2011a). Mass models of the Milky Way. *Monthly Notices of the Royal Astronomical Society, Volume 414, Issue 3, pp. 2446-2457.*, 414:2446–2457.
- McMillan, P. J. and J., P. (2011b). Mass models of the Milky Way. *Monthly Notices of the Royal Astronomical Society, Volume 414, Issue 3, pp. 2446-2457.*, 414:2446–2457.
- McMillan, P. J. and J., P. (2016). The mass distribution and gravitational potential

- of the Milky Way. *Monthly Notices of the Royal Astronomical Society, Volume 465, Issue 1, p.76-94*, 465:76–94.
- McWilliam, A. and Zoccali, M. (2010). Two Red Clumps and the X-Shaped Milky Way Bulge. *The Astrophysical Journal, Volume 724, Issue 2, pp. 1491-1502 (2010).*, 724:1491–1502.
- Nataf, D. M., Udalski, A., Gould, A., Fouque, P., and Stanek, K. Z. (2010). The Split Red Clump of the Galactic Bulge from OGLE-III. *The Astrophysical Journal Letters, Volume 721, Issue 1, pp. L28-L32 (2010).*, 721:L28–L32.
- Ness, M., Debattista, V. P., Bensby, T., Feltzing, S., Roškar, R., Cole, D. R., Johnson, J. A., and Freeman, K. (2014). YOUNG STARS IN AN OLD BULGE: A NATURAL OUTCOME OF INTERNAL EVOLUTION IN THE MILKY WAY. *The Astrophysical Journal*, 787(2):L19.
- Ness, M., Freeman, K., Athanassoula, E., de Boer, E. W., Hawthorn, J. B., Asplund, M., Lewis, G. F., Yong, D., Lane, R. R., and Kiss, L. L. (2012). ARGOS III: Stellar Populations in the Galactic Bulge of the Milky Way. *Monthly Notices of the Royal Astronomical Society, Volume 430, Issue 2, p.836-857*, 430:836–857.
- Nishiyama, S., Nagata, T., Kusakabe, N., Matsunaga, N., Naoi, T., Kato, D., Nagashima, C., Sugitani, K., Tamura, M., Tanabe, T., and Sato, S. (2006). Interstellar Extinction Law in the J, H, and Ks Bands toward the Galactic Center. *The Astrophysical Journal*, 638(2):839–846.
- Noguchi, M. (2000). Secular evolution of late-type disc galaxies: formation of bulges and the origin of bar dichotomy. *Monthly Notices of the Royal Astronomical Society*, 312(1):194–206.
- Ojha, D. K. and K., D. (2001). Radial scalelengths of the galactic thin and thick

- disc with 2MASS data. *Monthly Notices of the Royal Astronomical Society*, 322(2):426–432.
- Persic, M. and Salucci, P. (1992). The baryon content of the Universe. *Monthly Notices of the Royal Astronomical Society*, 258(1):14P–18P.
- Piatti, A. E. (2012). IDENTIFICATION OF A NEW RELATIVELY OLD STAR CLUSTER IN THE SMALL MAGELLANIC CLOUD. *The Astrophysical Journal*, 756(2):L32.
- Piatti, A. E. and Geisler, D. (2013). THE AGE-METALLICITY RELATIONSHIP OF THE LARGE MAGELLANIC CLOUD FIELD STAR POPULATION FROM WIDE-FIELD WASHINGTON PHOTOMETRY. *The Astronomical Journal*, 145(1):17.
- Pietrukowicz, P., Kozłowski, S., Skowron, J., Soszynski, I., Udalski, A., Poleski, R., Wyrzykowski, L., Szymanski, M. K., Pietrzynski, G., Ulaczyk, K., Mroz, P., Skowron, D. M., and Kubiak, M. (2014). Deciphering the 3D structure of the old Galactic bulge from the OGLE RR Lyrae stars. *The Astrophysical Journal*, Volume 811, Issue 2, article id. 113, 12 pp. (2015)., 811.
- Pontzen, A., Roškar, R., Stinson, G. S., Woods, R., Reed, D. M., Coles, J., and Quinn, T. R. (2013). pynbody: Astrophysics Simulation Analysis for Python. Astrophysics Source Code Library, ascl:1305.002.
- Portaluri, E., Corsini, E. M., Morelli, L., Hartmann, M., Dalla Bontà, E., De-
battista, V. P., and Pizzella, A. (2013). Searching for nuclear stellar discs in
simulations of star cluster mergers. *Monthly Notices of the Royal Astronomical
Society*, 433(1):434–444.
- Prugniel, P., Maubon, G., and Simien, F. (2001). The formation of galaxy bulges:
Spectrophotometric constraints. *Astronomy & Astrophysics*, 366(1):68–82.

- Qin, W., Nataf, D. M., Zakamska, N., Wood, P. R., and Casagrande, L. (2018). The Mira-based distance to the Galactic centre. *The Astrophysical Journal*, 865(1):47.
- Qin, Y., Shen, J., Li, Z.-Y., Mao, S., Smith, M. C., Rich, R. M., Kunder, A., and Liu, C. (2015). KINEMATICS OF THE X-SHAPED MILKY WAY BULGE: EXPECTATIONS FROM A SELF-CONSISTENT *N*-BODY MODEL. *The Astrophysical Journal*, 808(1):75.
- Quillen, A. C., Minchev, I., Sharma, S., Qin, Y.-J., and Di Matteo, P. (2013). A Vertical Resonance Heating Model for X- or Peanut-Shaped Galactic Bulges. *Monthly Notices of the Royal Astronomical Society, Volume 437, Issue 2, p.1284-1307*, 437:1284–1307.
- Raha, N., Sellwood, J. A., James, R. A., and Kahn, F. D. (1991). A dynamical instability of bars in disk galaxies. *Nature*, 352(6334):411–412.
- Rattenbury, N. J., Mao, S., Debattista, V. P., Sumi, T., Gerhard, O., and De Lorenzi, F. (2007a). Proper Motion Dispersions of Red Clump Giants in the Galactic Bulge: Observations and Model Comparisons. *Monthly Notices of the Royal Astronomical Society, Volume 378, Issue 3, pp. 1165-1176.*, 378:1165–1176.
- Rattenbury, N. J., Mao, S., Sumi, T., and Smith, M. C. (2007b). Modelling the Galactic bar using OGLE-II Red Clump Giant Stars. *Monthly Notices of the Royal Astronomical Society, Volume 378, Issue 3, pp. 1064-1078.*, 378:1064–1078.
- Robin, A. C., Marshall, D. J., Schultheis, M., and Reyle, C. (2011). Stellar populations in the Milky Way bulge region : Towards solving the Galactic bulge and bar shapes using 2MASS data. *Astronomy & Astrophysics, Volume 538, id.A106, 14 pp.*, 538.
- Roskar, R. and Debattista, V. P. (2012). Galactic Archaeology. *Science*, 338(6105):333–334.

- Roškar, R., Debattista, V. P., Stinson, G. S., Quinn, T. R., Kaufmann, T., and Wadsley, J. (2007). Beyond Inside-Out Growth: Formation and Evolution of Disk Outskirts. *The Astrophysical Journal Letters*, Volume 675, Issue 2, pp. L65 (2008)., 675:L65.
- Rubele, S., Girardi, L., Kerber, L., Cioni, M.-R. L., Piatti, A. E., Zaggia, S., Bekki, K., Bressan, A., Clementini, G., de Grijs, R., Emerson, J. P., Groenewegen, M. A. T., Ivanov, V. D., Marconi, M., Marigo, P., Moretti, M.-I., Ripepi, V., Subramanian, S., Tatton, B. L., and van Loon, J. T. (2015). The VMC survey - XIV. First results on the look-back time star formation rate tomography of the Small Magellanic Cloud. *Monthly Notices of the Royal Astronomical Society*, Volume 449, Issue 1, p.639-661, 449:639–661.
- Rubele, S., Kerber, L., Girardi, L., Cioni, M.-R., Marigo, P., Zaggia, S., Bekki, K., de Grijs, R., Emerson, J., Groenewegen, M. A. T., Gullieuszik, M., Ivanov, V., Miszalski, B., Oliveira, J. M., Tatton, B., and van Loon, J. T. (2012). The VMC survey. IV. The LMC star formation history and disk geometry from four VMC tiles. *Astronomy & Astrophysics*, Volume 537, id.A106, 19 pp., 537.
- Saha, K., Tseng, Y. H., and Taam, R. E. (2010). The effect of bars and transient spirals on the vertical heating in disk galaxies. *The Astrophysical Journal*, Volume 721, Issue 2, pp. 1878-1890 (2010)., 721:1878–1890.
- Saito, R. K., Hempel, M., Minniti, D., Lucas, P. W., Rejkuba, M., Toledo, I., Gonzalez, O. A., Alonso-Garcia, J., Irwin, M. J., Gonzalez-Solares, E., Hodgkin, S. T., Lewis, J. R., Cross, N., Ivanov, V. D., Kerins, E., Emerson, J. P., Soto, M., Amores, E. B., Gurovich, S., Dekany, I., Angeloni, R., Beamin, J. C., Catelan, M., Padilla, N., Zoccali, M., Pietrukowicz, P., Bidin, C. M., Mauro, F., Geisler, D., Folkes, S. L., Sale, S. E., Borissova, J., Kurtev, R., Ahumada, A. V., Alonso, M. V., Adamson, A., Arias, J. I., Bandyopadhyay, R. M., Barba, R. H., Barbuy,

- B., Baume, G. L., Bedin, L. R., Bellini, A., Benjamin, R., Bica, E., Bonatto, C., Bronfman, L., Carraro, G., Chene, A. N., Claria, J. J., Clarke, J. R. A., Contreras, C., Corvillon, A., de Grijs, R., Dias, B., Drew, J. E., Farina, C., Feinstein, C., Fernandez-Lajus, E., Gamen, R. C., Gieren, W., Goldman, B., Gonzalez-Fernandez, C., Grand, R. J. J., Gunthardt, G., Hambly, N. C., Hanson, M. M., Helminiak, K. G., Hoare, M. G., Huckvale, L., Jordan, A., Kinemuchi, K., Longmore, A., Lopez-Corredoira, M., Maccarone, T., Majaess, D., Martin, E. L., Masetti, N., Mennickent, R. E., Mirabel, I. F., Monaco, L., Morelli, L., Motta, V., Palma, T., Parisi, M. C., Parker, Q., Penaloza, F., Pietrzynski, G., Pignata, G., Popescu, B., Read, M. A., Rojas, A., Roman-Lopes, A., Ruiz, M. T., Saviane, I., Schreiber, M. R., Schroder, A. C., Sharma, S., Smith, M. D., Sodre, L., Stead, J., Stephens, A. W., Tamura, M., Tappert, C., Thompson, M. A., Valenti, E., Vanzi, L., Walton, N. A., Weidmann, W., and Zijlstra, A. (2011a). VVV DR1: The First Data Release of the Milky Way Bulge and Southern Plane from the Near-Infrared ESO Public Survey VISTA Variables in the Via Lactea. *Astronomy & Astrophysics, Volume 537, id.A107, 21 pp.*, 537.
- Saito, R. K., Zoccali, M., McWilliam, A., Minniti, D., Gonzalez, O. A., and Hill, V. (2011b). Mapping the X-Shaped Milky Way Bulge. *The Astronomical Journal, Volume 142, Issue 3, article id. 76, 6 pp. (2011).*, 142.
- Sanders, J. L., Smith, L., Evans, N. W., and Lucas, P. (2019). Transverse kinematics of the Galactic bar-bulge from VVV and Gaia. *Monthly Notices of the Royal Astronomical Society*, 487(4):5188–5208.
- Sellwood, J. A. and A., J. (1985). The global stability of our Galaxy. *Monthly Notices of the Royal Astronomical Society*, 217(1):127–148.
- Sersic, J. L. (1968). Atlas de Galaxias Australes. *Cordoba, Argentina: Observatorio Astronomico, 1968.*

- Stanek, K. Z., Mateo, M., Udalski, A., Szymanski, M., Kaluzny, J., Kubiak, M., Stanek, K. Z., Mateo, M., Udalski, A., Szymanski, M., Kaluzny, J., and Kubiak, M. (1994). Color-Magnitude Diagram Distribution of the Bulge Red Clump Stars - Evidence for the Galactic Bar. *The Astrophysical Journal*, 429:L73.
- Stanek, K. Z., Udalski, A., Szymanski, M., Kaluzny, J., Kubiak, M., Mateo, M., and Krzeminski, W. (1996). Modelling the Galactic Bar Using Red Clump Giants. *The Astrophysical Journal*, Volume 477, Issue 1, pp. 163-175., 477:163–175.
- Stanek, K. Z., Udalski, A., Szymański, M., Kałużny, J., Kubiak, Z. M., Mateo, M., and Krzemiński, W. (1997). Modeling the Galactic Bar Using Red Clump Giants. *The Astrophysical Journal*, 477(1):163–175.
- Stinson, G., Seth, A., Katz, N., Wadsley, J., Governato, F., and Quinn, T. (2006). Star Formation and Feedback in Smoothed Particle Hydrodynamic Simulations— I. Isolated Galaxies. *Monthly Notices of the Royal Astronomical Society*, Volume 373, Issue 3, pp. 1074-1090., 373:1074–1090.
- Sumi, T. and Takahiro (2003). Extinction Map of the Galactic center: OGLE-II Galactic bulge fields. *Monthly Notices of the Royal Astronomical Society*, Volume 349, Issue 1, pp. 193-204., 349:193–204.
- Valenti, E., Zoccali, M., Gonzalez, O. A., Minniti, D., Alonso-Garcia, J., Marchetti, E., Hempel, M., Renzini, A., and Rejkuba, M. (2015). Stellar density profile and mass of the Milky Way Bulge from VVV data. *Astronomy & Astrophysics*, Volume 587, id.L6, 4 pp., 587.
- Valluri, M., Shen, J., Abbott, C., and Debattista, V. P. (2016). A UNIFIED FRAMEWORK FOR THE ORBITAL STRUCTURE OF BARS AND TRIAXIAL ELLIPSOIDS. *The Astrophysical Journal*, 818(2):141.

- Wadsley, J., Stadel, J., and Quinn, T. (2003). Gasoline: An adaptable implementation of TreeSPH. *New Astronomy, Volume 9, Issue 2, p. 137-158.*, 9:137–158.
- Wegg, C. and Gerhard, O. (2013). Mapping the Three-Dimensional Density of the Galactic Bulge with VVV Red Clump Stars. *Monthly Notices of the Royal Astronomical Society, Volume 435, Issue 3, p.1874-1887*, 435:1874–1887.
- Wegg, C., Gerhard, O., and Portail, M. (2015). The Structure of the Milky Way’s Bar Outside the Bulge. *Monthly Notices of the Royal Astronomical Society, Volume 450, Issue 4, p.4050-4069*, 450:4050–4069.
- Woosley, S. E. and Weaver, T. A. (1995). The Evolution and Explosion of Massive Stars. II. Explosive Hydrodynamics and Nucleosynthesis. *The Astrophysical Journal Supplement Series*, 101:181.
- Zoccali, M. and Valenti, E. (2016). The 3D Structure of the Galactic Bulge. *Publications of the Astronomical Society of Australia*, 33:e025.
- Zoccali, M., Vasquez, S., Gonzalez, O. A., Valenti, E., Rojas-Arriagada, A., Minniti, J., Rejkuba, M., Minniti, D., McWilliam, A., Babusiaux, C., Hill, V., and Renzini, A. (2017). The GIRAFFE Inner Bulge Survey (GIBS) III. Metallicity distributions and kinematics of 26 Galactic bulge fields. *Astronomy & Astrophysics, Volume 599, id.A12, 13 pp.*, 599.